Fig. 4

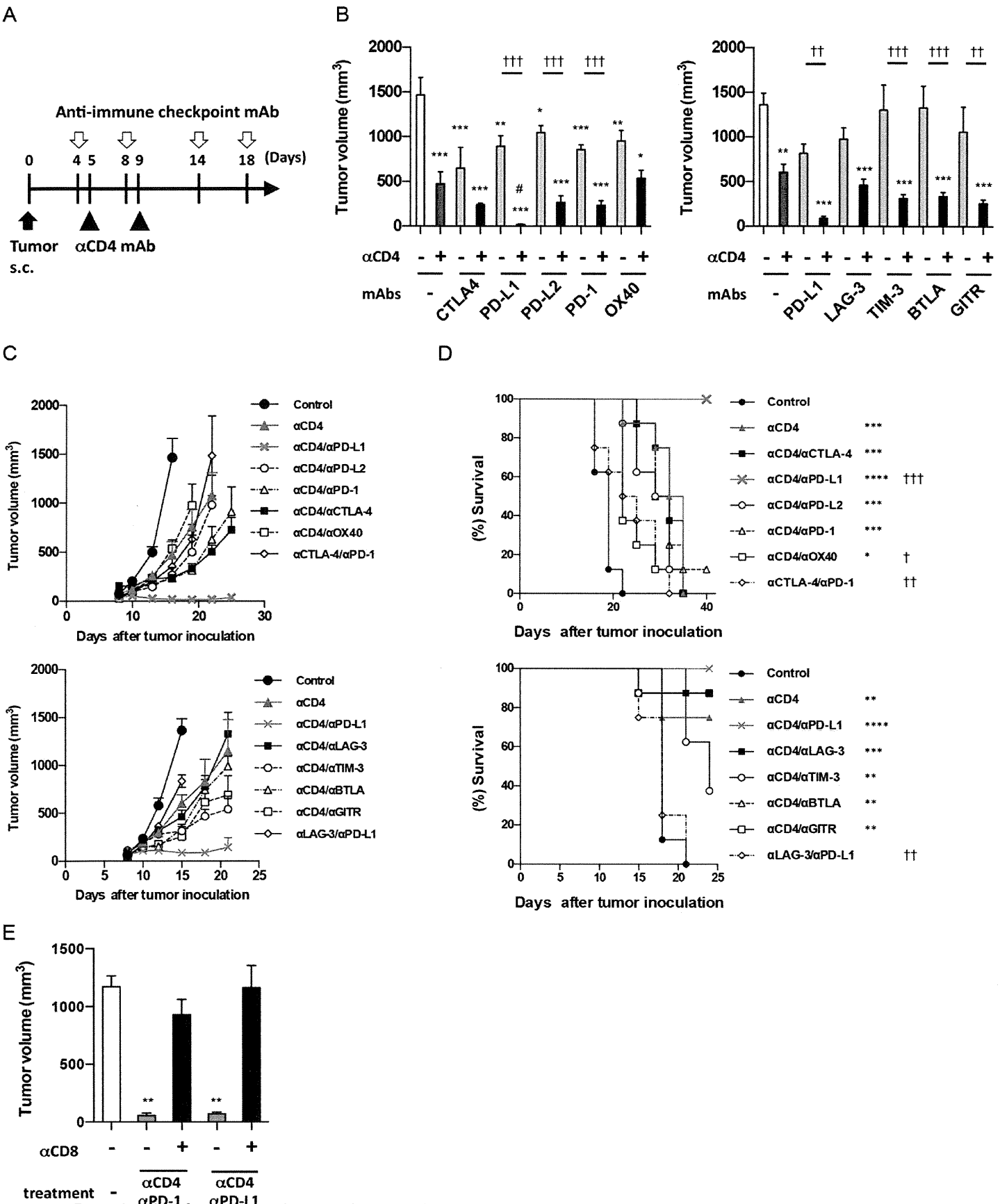

Author Manuscript Published OnlineFirst on February 20, 2015; DOI: 10.1158/2326-6066.CIR-14-0190
Author manuscripts have been peer reviewed and accepted for publication but have not yet been edited.

Fig. 5

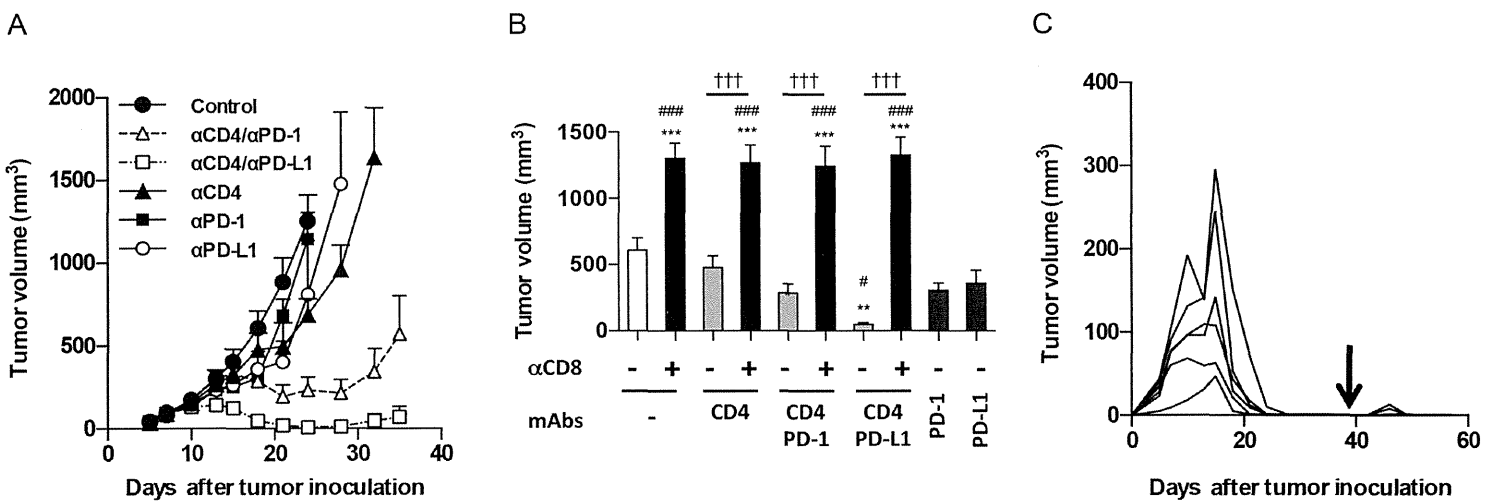

Author Manuscript Published OnlineFirst on February 20, 2015; DOI: 10.1158/2326-6066.CIR-14-0190
Author manuscripts have been peer reviewed and accepted for publication but have not yet been edited.

Fig. 6

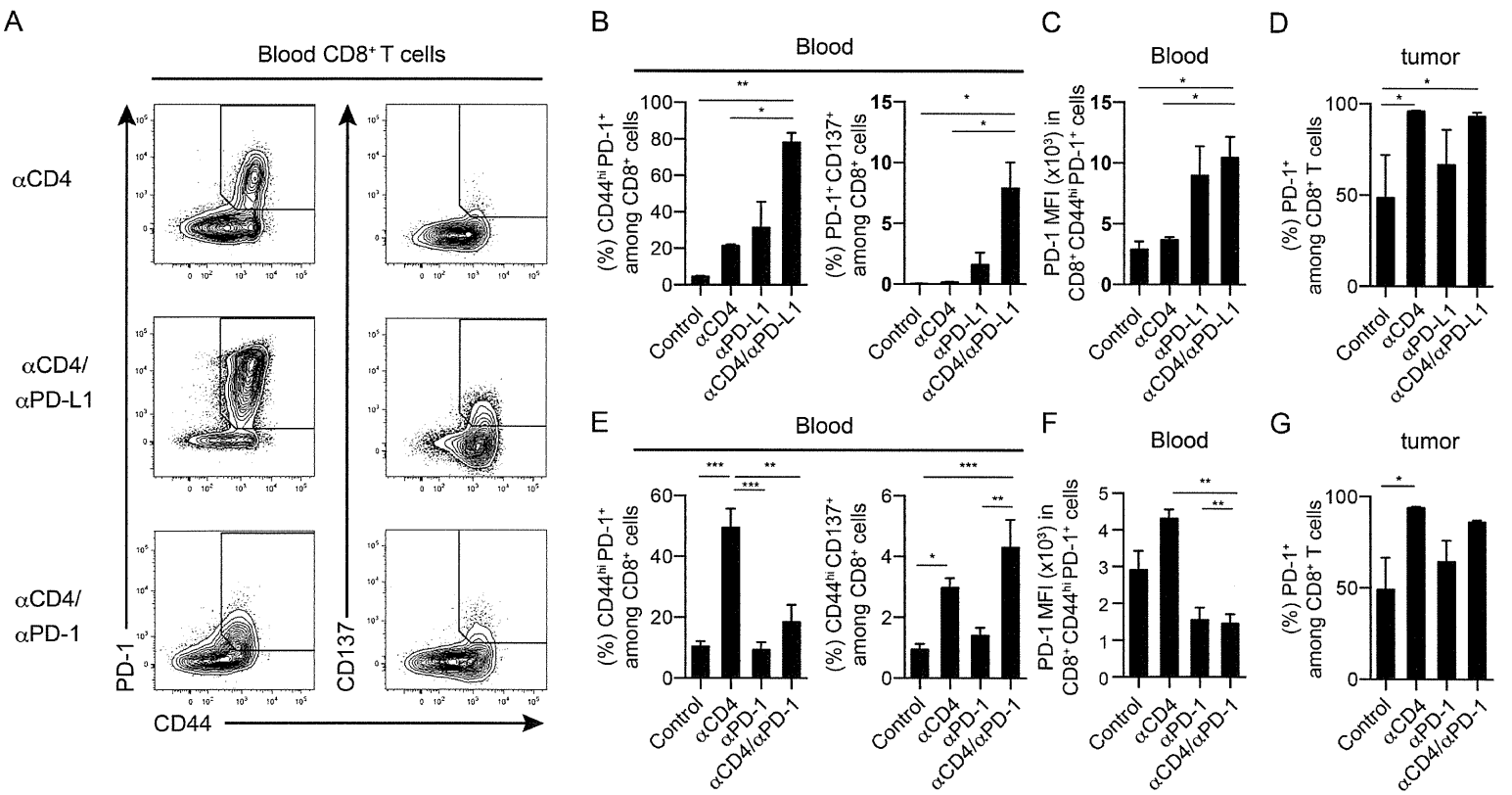

AACR American Association for Cancer Research

Cancer Immunology Research

Robust anti-tumor effects of combined anti-CD4 depleting antibody and anti-PD-1/PD-L1 immune checkpoint antibody treatment in mice

Satoshi Ueha, Shoji Yokochi, Yoshiro Ishiwata, et al.

Cancer Immunol Res Published OnlineFirst February 20, 2015.

Published OnlineFirst August 15, 2014; DOI: 10.1158/2326-6066.CIR-14-0098

Research Article

Cancer Immunology Research

Cytotoxic T Lymphocytes Block Tumor Growth Both by Lytic Activity and IFNγ-Dependent Cell-Cycle Arrest

Hirokazu Matsushita[1], Akihiro Hosoi[1,2], Satoshi Ueha[3], Jun Abe[3], Nao Fujieda[1,2], Michio Tomura[4], Ryuji Maekawa[2], Kouji Matsushima[3], Osamu Ohara[5], and Kazuhiro Kakimi[1]

Abstract

To understand global effector mechanisms of CTL therapy, we performed microarray gene expression analysis in a murine model using pmel-1 T-cell receptor (TCR) transgenic T cells as effectors and B16 melanoma cells as targets. In addition to upregulation of genes related to antigen presentation and the MHC class I pathway, and cytotoxic effector molecules, cell-cycle–promoting genes were downregulated in the tumor on days 3 and 5 after CTL transfer. To investigate the impact of CTL therapy on the cell cycle of tumor cells *in situ*, we generated B16 cells expressing a fluorescent ubiquitination-based cell-cycle indicator (B16-fucci) and performed CTL therapy in mice bearing B16-fucci tumors. Three days after CTL transfer, we observed diffuse infiltration of CTLs into the tumor with a large number of tumor cells arrested at the G_1 phase of the cell cycle, and the presence of spotty apoptotic or necrotic areas. Thus, tumor growth suppression was largely dependent on G_1 cell-cycle arrest rather than killing by CTLs. Neutralizing antibody to IFNγ prevented both tumor growth inhibition and G_1 arrest. The mechanism of G_1 arrest involved the downregulation of S-phase kinase-associated protein 2 (Skp2) and the accumulation of its target cyclin-dependent kinase inhibitor p27 in the B16-fucci tumor cells. Because tumor-infiltrating CTLs are far fewer in number than the tumor cells, we propose that CTLs predominantly regulate tumor growth via IFNγ-mediated profound cytostatic effects rather than via cytotoxicity. This dominance of G_1 arrest over other mechanisms may be widespread but not universal because IFNγ sensitivity varied among tumors. *Cancer Immunol Res; 3(1); 26–36. ©2014 AACR.*

See related commentary by Riddell, p. 23

Introduction

Adoptive T-cell immunotherapy (ACT) using autologous tumor-infiltrating lymphocytes (TIL) can be highly effective for treating melanoma (1). The recent development of genetically engineered T cells stably expressing exogenous T-cell receptors (TCR) or chimeric antigen receptors (CAR) specific for tumor-associated antigens offers the possibility of testing the efficacy of ACT against a wide range of cancer types in addition to melanoma (2, 3). Many clinical trials have now been conducted using genetically engineered T cells specific for tumor antigens as well as TILs, and some objective responses have been achieved (4, 5). It is clear from mouse models that adoptively transferred antigen-specific T cells are capable of eradicating established cancer (6–8), and the ability of CTLs to directly kill tumor and/or stromal cells is thought to be important for tumor elimination (9–11). Nonetheless, cytokines such as IFNγ and TNFα produced by T cells are also likely to contribute to the prevention of tumor growth by ACT via mechanisms other than cell lysis (12–14).

IFNγ is a critical cytokine for antitumor immunity under natural and therapeutic conditions (15, 16). It enhances tumor immunogenicity by upregulating components of the MHC antigen processing and presentation pathway. It also induces the expression of chemokines, including the angiostatic chemokines CXCL9 (MIG), CXCL10 (IP-10), and CXCL11 (I-TAC), that block neovascularization in the tumor and recruit effector immune cells (17–19). Furthermore, IFNγ has been reported to exert antiproliferative effects on the developing tumor (20, 21), and it triggers apoptosis of tumor cells by inducing proapoptotic molecules (22, 23).

To understand the global antitumor effect mediated by ACT, we used the B16 melanoma pmel-1 TCR-transgenic T-cell model to perform a gene expression analysis of ACT-treated tumors. On the basis of these results, we focused on genes controlling the cell cycle and arresting growth of B16 tumor cells in this model. We examined the effects on tumor cells of the IFNγ produced by the CTLs *in situ* using cell-cycle status indicators and investigated the mechanism of cell-cycle arrest. Furthermore, we demonstrate the importance of cell-cycle arrest induced by CTL-derived IFNγ in the regulation of tumor growth.

[1]Department of Immunotherapeutics, The University of Tokyo Hospital, Tokyo, Japan. [2]Medinet Co Ltd., Yokohama, Japan. [3]Department of Molecular Preventive Medicine, Graduate School of Medicine, The University of Tokyo, Tokyo, Japan. [4]Center for Innovation in Immunoregulative Technology and Therapeutics, Kyoto University Graduate School of Medicine, Kyoto, Japan. [5]Department of Human Genome Research, Kazusa DNA Research Institute, Chiba, Japan.

Note: Supplementary data for this article are available at Cancer Immunology Research Online (http://cancerimmunolres.aacrjournals.org/).

Corresponding Author: Kazuhiro Kakimi, Department of Immunotherapeutics, The University of Tokyo Hospital, 7-3-1 Hongo, Bunkyo-Ku, Tokyo 113-8655, Japan. Phone: 81-3-5805-3161; Fax: 81-3-5805-3164; E-mail: kakimi@m.u-tokyo.ac.jp

doi: 10.1158/2326-6066.CIR-14-0098

Published OnlineFirst August 15, 2014; DOI: 10.1158/2326-6066.CIR-14-0098

Materials and Methods

Mice, tumor cells, and peptides

Six-week-old male C57BL/6 mice were purchased from Japan SLC. Mice transgenic for the pmel-1-TCR, which recognizes the H-2D^b–restricted epitope EGSRNQDWL from gp100 (gp100$_{25-33}$), were obtained from The Jackson Laboratory. All mice were housed in a pathogen-free environment, and all animal procedures were conducted in accordance with institutional guidelines. All animal experiments were approved by the University of Tokyo Ethics Committee for Animal Experiments (10-P-127). The H-2D^b–restricted peptide human gp100 (hgp100$_{25-33}$, KVPRNQDWL) was purchased from GenScript Japan at a purity of >90%, with free amino and carboxyl terminals. B16F10, FBL3, and 3LL cell lines were maintained in culture medium consisting of DMEM with 10% FCS, 100 U/mL penicillin, and 100 μg/mL streptomycin. EL4, P815, and CT26 were cultured in RPMI-1640 medium supplemented with 10% FCS, 100 U/mL penicillin, and 100 μg/mL streptomycin. All cell lines were tested for Mycoplasma by the MycoAlert Mycoplasma Detection kit (Lonza). Cellular morphology and growth curve *in vitro* were checked in all cell lines. B16F10 and B16-fucci cells were authenticated by transplantation for assessing growth ability *in vivo*.

Dendritic cell preparation and CTL stimulation

Dendritic cells (DC) were obtained by 8-day culture of C57BL/6-derived bone marrow cells with granulocyte-macrophage colony-stimulating factor (GM-CSF), as described previously (24). Briefly, bone marrow cells obtained from tibias and femurs of C57BL/6 mice were cultured in RPMI-1640 medium supplemented with 10% FCS, 10 mmol/L HEPES, 5×10^{-5} mol/L 2-mercaptoethanol, 1×10^{-3} mol/L sodium pyruvate, 1% nonessential amino acids, 100 U/mL penicillin, 100 μg/mL streptomycin, and 20 ng/mL GM-CSF (PeproTech) for 8 days. On days 3 and 6, half of the medium was replaced with fresh medium containing GM-CSF. DCs were further incubated with 1 μg/mL lipopolysaccharide for 16 hours and then pulsed with 1 μg/mL hgp100 peptide for 3 hours to obtain mature DCs. To prepare CTLs, 1×10^7 spleen cells from pmel-1 TCR-transgenic mice were cocultured with 2×10^5 DCs in a medium containing 50 U/mL IL2 (Chiron Corporation). After 3 days of *in vitro* stimulation, approximately 90% of the harvested cells were CD3$^+$CD8$^+$ CTLs.

ACT and anti-IFNγ mAb treatment

C57BL/6 mice were inoculated subcutaneously with 1×10^6 B16 tumor cells followed by adoptive CTL transfer (1×10^7 or 4×10^7) 9 days later. Tumor growth was monitored every 2 to 3 days with calipers in an anonymous fashion. On the day of, and 2 days after, CTL transfer, mice received intraperitoneal injections of 500 μg anti-IFNγ mAb (clone XMG1.2; BioXCell) or rat IgG$_1$ isotype control (BioXCell). Tumor volume was calculated as described previously (24).

Cell preparation and flow cytometry

Tumors were harvested from mice at scheduled time points, cut into pieces, and resuspended in Hank's Balanced Salt Solution (HBSS) supplemented with 0.1% collagenase D (Roche Diagnostics) and DNase I (Roche Diagnostics) for 60 minutes at 37°C. The entire mass of the material was pressed through a 70-μm cell strainer (BD Falcon; BD Biosciences) using a plunger to obtain single-cell suspensions of tumor-infiltrating cells. For flow cytometry, the cells were first stained with the Fixable Viability Dye eFluor450 (eBioscience) to label dead cells, and pretreated with Fc Block (anti-CD16/32 clone 2.4G2; BD Pharmingen). The cells were then stained with antibodies and analyzed on a Gallios flow cytometer (Beckman Coulter). The following mAbs were obtained from BioLegend: PerCP/Cy5.5-conjugated anti-CD45, Alexa Fluor647–conjugated anti-CD90.1, and APC-Cy7–conjugated anti-CD8. Data were analyzed with the Kaluza software (Beckman Coulter).

Comprehensive gene expression analysis

Gene expression profiling data of B16 tumor tissues on different days were obtained by Agilent whole-mouse genome microarray. Total RNA was extracted with TRizol (Invitrogen) from B16 tumor tissues and fluorescently labeled using a One-Color Agilent Quick Amp Labeling Kit. The microarray slides were hybridized, washed, and read on an Agilent Microarray scanner following the manufacturer's instructions, and raw fluorescence signal intensities were generated by Agilent Feature Extraction Software v9.5. The signals were normalized to align at 75th percentile, and then turned into $\log_2$ ratio against day 1 in untreated and CTL-treated groups. We began with 45,018 probes, and removed probes if their gIsWellAboveBG flag values were 0 at all samples, and then filtered out $\log_2$ ratio values that were unvarying (between −1 and 1) at all time points. We obtained 10,855 probes and ran hierarchical clustering (standard correlation, UPGMA) on them. All data were analyzed with the Subio Platform and Basic Plug-in v1.16 (Subio Inc.). The microarray data are available from the Gene Expression Omnibus (GEO) database (series accession number GSE57304; sample accession numbers GSM1379331–GSM1379344).

For quantitative gene panel–based PCR, Cell Cycle RT^2 *Profiler* PCR arrays (SABioscience; http://www.sabiosciences.com/rt_pcr_product/HTML/PAMM-020Z.html) were used to simultaneously examine the mRNA levels of 84 genes in 96-well PCR array plates. Total RNA was prepared using TRizol according to the manufacturer's instructions (Invitrogen), and reverse-transcribed using RT2 First Strand kits (SABioscience). Real-time PCR was performed as instructed by the supplier on an ABI PRISM 7900HT Sequence Detection System (Life Technologies). Data were analyzed by a ΔΔ cycle threshold method to determine the fold changes of the mRNA levels (http://www.SABiosciences.com/pcrarraydataanalysis.php).

Expression vectors

CSII-EF-MCS/mAG-hGeminin and CSII-EF-MCS/mKO-cdt1 vectors were kindly provided by Dr. Atsushi Miyawaki (RIKEN, Wako, Japan; ref. 25). cDNA encoding mouse *IFNGR1* lacking the intracellular component of the receptor (26) was generated by PCR using the primer pair 5′-ATCTCACTCGAGATGGGCCCG-CAGGCGGCAGCT-3′ and 5′-ATCTCAGAATTCATTCTTCTTAG-TATACCAATA-3′ and subcloned into the *Xho*-1 and *Eco*-RI sites of the RV-GFP vector (designated RV-IFNGR1ΔIC; ref. 27).

Production of B16-fucci and B16-fucciΔIC tumor cells

mAG-hGeminin and mKO-cdt1 were expressed in B16 tumor cells using lentiviral vectors (designated B16-fucci). IFNGR1 lacking the sequence encoding the intracellular component of the receptor was expressed in B16-fucci tumor cells in the same way (designated B16-fucciΔIC).

Published OnlineFirst August 15, 2014; DOI: 10.1158/2326-6066.CIR-14-0098

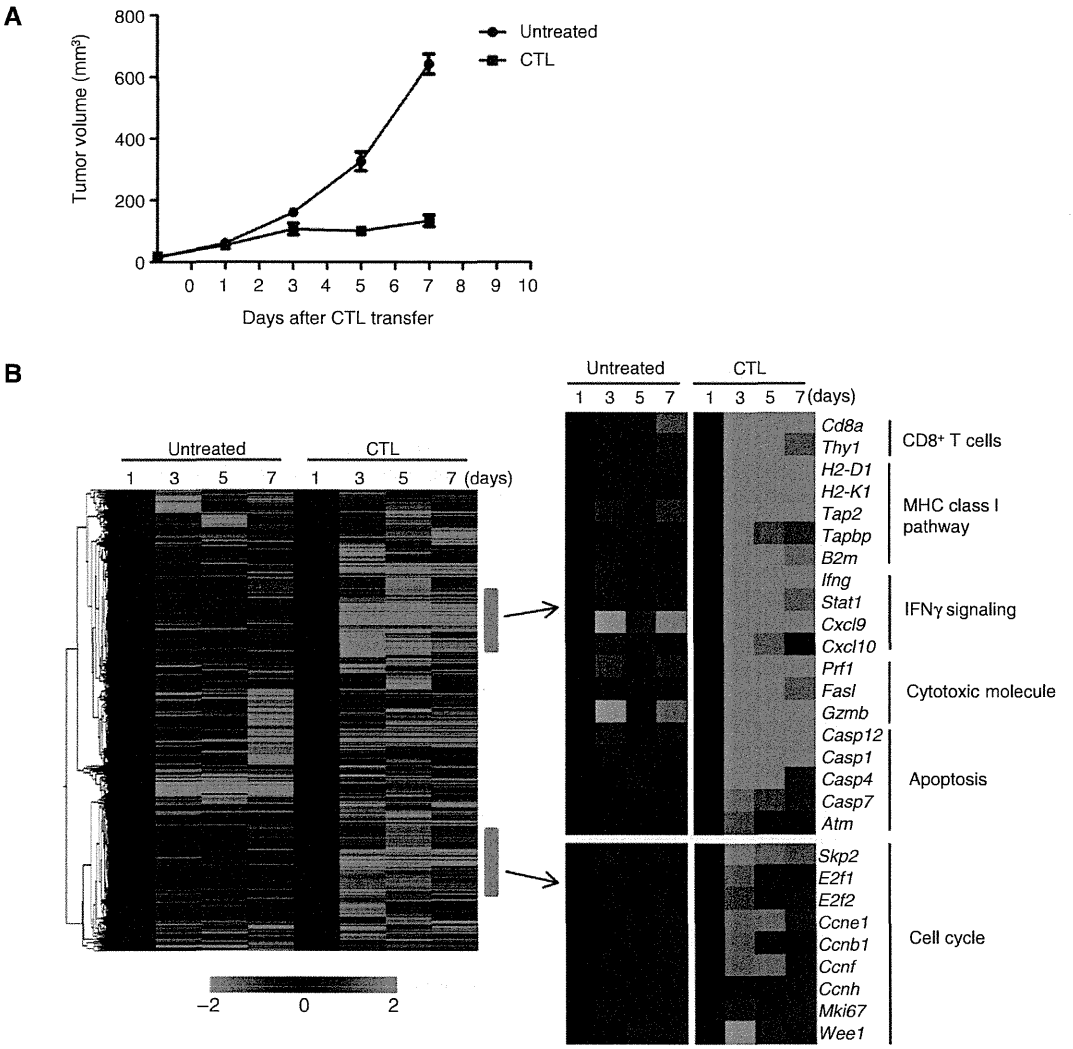

C

Genes	fold regulation	*P*
Skp2	−2.786	0.00009
E2f2	−2.7508	0.011257
Ccnb2 (Cyclin B2)	−2.1494	0.001346
Ccnf (Cyclin F)	−2.0253	0.002599
Mki67	−2.359	0.006258
Rad51	−2.3885	0.00095
Wee1	−2.4354	0.000533

Figure 1.
Gene expression analysis of the tumor in ACT. A, C57BL/6 mice were injected with 1×10^6 B16 tumor cells, and 9 days later (designated as day 0), tumor-bearing mice received 1×10^7 *in vitro* activated B16-specific (gp100-specific) CD90.1$^+$ CTLs (designated ACT mice). Tumor volumes were measured on days 1, 3, 5, and 7 after CTL transfer ($n = 5$). B, tumor tissues from untreated or ACT mice were harvested on days 1, 3, 5, and 7. Total RNA extracted from 3 to 4 tumor tissues in each group was pooled and used for gene expression analysis. Heatmaps of hierarchical clustering analysis based on fold changes of gene expression on days 3, 5, and 7 relative to day 1 are shown (left). Some groups of genes that were upregulated (top) or downregulated (bottom) after CTL transfer were extracted (right). C, cell-cycle PCR array performed using tumor tissues from untreated or ACT mice ($n = 4$) on day 3. Seven cell-cycle genes that were significantly downregulated in the tumors from ACT mice are shown. The fold regulation is the negative inverse of the fold change.

Published OnlineFirst August 15, 2014; DOI: 10.1158/2326-6066.CIR-14-0098

Quantitative RT-PCR

Total RNA was extracted using TRizol and converted into cDNA using the SuperScript III First-Strand Synthesis System according to the manufacturer's instructions (Invitrogen). Quantitative RT-PCR (qRT-PCR) reactions were carried out using EXPRESS SYBR GreenER qPCR SuperMix Universal (Invitrogen). Primer sequences are listed in Supplementary Table S1. PCR reactions were run in a Thermal Cycler Dice Real-Time System TP800 (TaKaRa) using the following program: one cycle of 95°C for 2 minutes, 40 cycles at 95°C for 15 seconds, and 60°C for 30 seconds. Results are expressed as ratios. The quantity of target mRNA was normalized to the level of GAPDH in each sample. PCR was performed in duplicate for each experiment, and PCR products were monitored by electrophoresis in 1.8% agarose gels and visualized with ethidium bromide.

Histologic analysis

Cryosections were fixed in 4% paraformaldehyde (PFA) at 4°C overnight and then transferred into 30% sucrose/PBS. After incubation for more than 24 hours, they were embedded in an optimal cutting temperature (OCT) compound (Sakura Finetek Japan) in liquid nitrogen. Sections measuring 8–10 μm were incubated with primary antibodies, followed by secondary antibodies and streptavidin. Polyclonal anti–Azami-Green antibody (PM011) was purchased from MBL. Polyclonal anti–single-stranded DNA was purchased from IBL-America. APC-conjugated anti-CD90.1 antibody was purchased from BD Biosciences. Alexa 647–conjugated polyclonal secondary antibodies and streptavidin were from Life Technologies. Anti-APC-biotin was from BioLegend. The samples were analyzed using a BZ-9000 fluorescence microscope with BZ-II image processing software (Keyence). The number of cells in the necrotic/apoptotic area was estimated by calculating the surface area of the region using BZ-H1M software (Keyence).

Cytology

Cultured B16-fucci tumor cells treated with IFNγ were examined using bright-field or fluorescence microscopy (Olympus IX71; Olympus; magnification, ×200).

Senescence-associated β-galactosidase activity assay

Senescence-associated β-galactosidase (SA-β-gal) activity in cancer cells was assessed using the Senescence Detection Kit (BioVision). SA-β-gal–positive cells were identified using bright-field microscopy (Olympus IX71; Olympus; magnification, ×400).

Protein extraction and Western blotting

B16-fucci tumors were harvested from untreated or ACT mice receiving either rat IgG (control for treatment) or anti-IFNγ mAb on day 3 after CTL transfer. Protein extracts were prepared from each tissue using RIPA buffer (Thermo Scientific) with the protease inhibitor cocktail Complete Mini (Roche). Protein extracts (50 μg) were used for immunoblotting. Protein extracts (30–50 μg) from B16-fucci, B16-fucciΔIC cells, FBL3-, or EL4-treated with IFNγ (10 U/mL) for the indicated time were used for immunoblotting. The following antibodies, all from Santa Cruz Biotechnology, were used: rabbit anti-pSTAT1 (sc-7988-R), rabbit anti-Skp2 (sc-7164), mouse anti-ATM (sc-23921), rabbit anti-p53ser15 (sc-101762), and rabbit anti-p21 (sc-397). Mouse anti-p27 (kip1) antibody was purchased from BD Biosciences. All antibodies were used at a final concentration of 0.2 to 1.0 μg/mL. After incubation with anti-rabbit IgG or anti-mouse IgG antibodies conjugated with horseradish peroxidase, proteins were visualized using the ECL Plus Western Blotting Detection System (GE Healthcare Life Sciences).

Statistical analysis

Comparison of results was performed by an unpaired, two-tailed Student *t* test with GraphPad Prism 5 (GraphPad Software, Inc.).

Results

Gene expression analysis in CTL transfer therapy

To understand the effector mechanism whereby ACT inhibits tumor growth, we assessed tumor-cell gene expression in a B16 melanoma model of pmel-1 TCR-transgenic CTL transfer. Tumors grew progressively in untreated B16-bearing mice, which was prevented between days 3 and 7 after the animals had received 10 million CTLs (Fig. 1A and Supplementary Fig. S1A). Tumor tissues were harvested from untreated mice and ACT mice on days 1, 3, 5, and 7 after CTL transfer, and gene expression was analyzed. Upregulation of genes related to $CD8^+$ T cells, the MHC class I pathway, IFNγ signaling, cytotoxic effector molecules, and others was observed in tumors from treated but not untreated mice (Fig. 1B). These data are consistent with our previous findings (24, 28) that adoptively transferred CTLs infiltrated into the tumor and that mRNA encoding *IFNγ*, *Perforin*, *Granzyme B*, and *FasL* was expressed on days 3 to 7, with kinetics reflecting the infiltration of the CTLs (Supplementary Fig. S1B and S1C).

Interestingly, some genes positively regulating the cell cycle, such as *Skp2*, *E2f2*, *Ccnf*, *Mki67*, and *Wee1*, were downregulated in tumors from ACT mice on days 3 and 5 (Fig. 1B). This was not the case in the untreated controls. We confirmed these data by a cell-cycle PCR array (Fig. 1C). Thus, gene expression analysis revealed profiles related to cell-cycle regulation, as well as cytotoxicity, in tumors from mice with ACT treatment.

CTL therapy induces G_1 cell-cycle arrest

Using the fucci (fluorescent ubiquitination-based cell-cycle indicator) system (25), we investigated the impact of ACT on the cell cycle of B16 tumor cells. To this end, we generated B16 tumor cells expressing fucci (designated B16-fucci), which emit red fluorescence in the G_1-phase, but otherwise fluoresce green. We then treated B16-fucci tumor-bearing mice with ACT. Tumor growth was not affected by the transduction of fucci into B16 tumor cells, but ACT inhibited their growth (Fig. 2A). On day 3 after CTL transfer, tumors were harvested from untreated or ACT mice for histologic analysis. As shown in Fig. 2B, CTLs had infiltrated into the tumors and were visible as blue spots. Whereas green cells were dominant in the growing tumor cells, the majority of tumor cells from ACT mice were red, suggesting that CTL therapy induced tumor cell-cycle arrest in the G_1-phase. Expressing the cell-cycle state as a green:red (G:R) ratio (Fig. 2C) showed that this was lower in the ACT mice (0.26 ± 0.12; $n = 3$) than in the untreated control mice on day 3 (1.1 ± 0.05; $n = 3$; $P = 0.0032$). This difference remained up to day 5 after CTL transfer, but on day 7, the G:R ratio increased again, together with the disappearance of CTLs, and green cells became dominant once more after day 10 (Supplementary Fig. S1B).

Published OnlineFirst August 15, 2014; DOI: 10.1158/2326-6066.CIR-14-0098

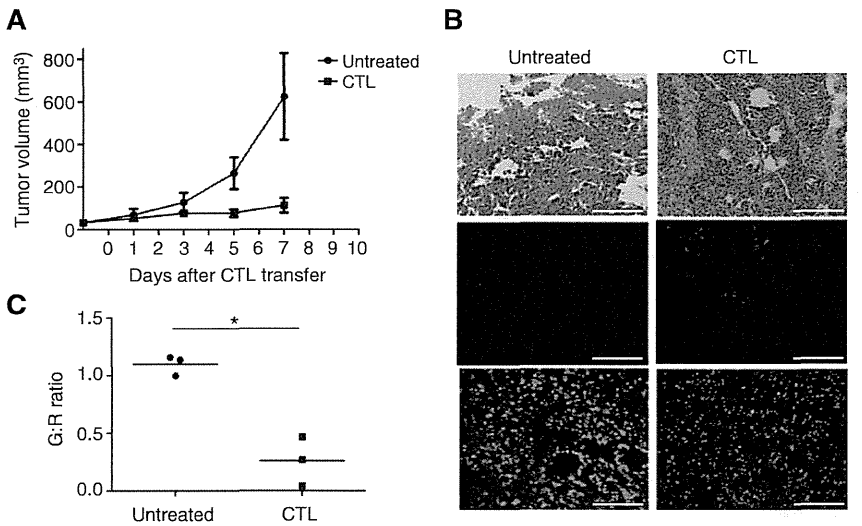

Figure 2.
CTL transfer therapy induced G_1 cell-cycle arrest of the tumor. A, C57BL/6 mice were injected with 1×10^6 B16-fucci tumor cells, and 9 days later, tumor-bearing mice ($n = 5$) were treated as described in Fig. 1. B, representative hematoxylin and eosin (top) and fluorescence microscopy images (middle and bottom) of cryosections of B16-fucci on day 3 ($n = 3$ per group). Alexa Fluor647–labeled anti-mouse CD90.1 antibody was used to detect infiltrating $CD90.1^+$ T cells (blue cells; middle). Scale bars, 200 μm. C, analysis of cell-cycle stage was performed by calculating the G:R ratio in fluorescence images ($n = 3$ per group). Samples were compared using an unpaired, two-tailed Student *t* test (*, $P < 0.01$).

IFNγ is critical for tumor growth inhibition and cell-cycle arrest

IFNγ is important for antitumor immunity. We have shown that it is critical for tumor growth inhibition in this model using IFNγ neutralizing antibody (anti-IFNγ mAb; ref. 28). Because IFNγ is involved in MHC class I upregulation, antigen processing, and trafficking of T cells into the tumor site by promoting chemokine production, the number of T cells infiltrating into the tumor was decreased by neutralizing IFNγ (data not shown). It was necessary to inject 4-fold more T cells to achieve the same level of CTL infiltration in anti-IFNγ Ab-treated animals (Fig. 3B). Nevertheless, anti-IFNγ treatment still prevented tumor growth blockade, despite the presence of equivalent levels of CTL in the tumor (Fig. 3A). Strikingly, this was the case even though the expression of mRNA encoding the effector molecules *IFNγ*, *Perforin*, *Granzyme B*, and *FasL* in ACT mice treated with anti-IFNγ mAb was the same or even higher than that in control ACT mice treated with rat IgG (Fig. 3C and D). A major difference in the anti-IFNγ mAb-treated mice was that the expression of mRNA encoding *STAT1* and IFNγ-inducible genes such as *MIG*, *IP10*, or *I-TAC* was suppressed. This suggests that IFNγ signaling was blocked by the treatment with anti-IFNγ mAb.

As shown in Fig. 4A, all tumor cells fluoresced either green or red. In growing tumors, the majority of B16 tumor cells were in the $S–G_2–M$ phase (Fig. 4A, left). After CTL transfer, most of the tumor cells became red (Fig. 4A, middle), but in the anti-IFNγ mAb-treated ACT mice, the tumor cells remained green (Fig. 4A, right). Diffused infiltration of CTLs into the tumor accompanied by massively infiltrated mononuclear cells and destruction of tumor cells, corresponding to spotty necrotic/apoptotic areas, was seen in ACT mice whether or not they received anti-IFNγ mAb treatment. Furthermore, apoptotic cells positive for single-stranded DNA (ssDNA), detected as white spots, were rare, but were present equally in ACT mice with or without anti-IFNγ mAb treatment (Fig. 4B and C). This, therefore, suggests that the transferred CTLs actually mediated relatively little tumor cell killing, which was unaffected by anti-IFNγ mAb administration.

The numbers of CTLs, tumor cells in necrotic/apoptotic areas, and tumor cells in the G_1 or $S–G_2–M$ phase were compared systematically in these mice. More green than red cells were observed in untreated tumors (Fig. 4D). In CTL-treated tumors, as described above, the G:R ratio was inverted, but the ratio was restored by the abrogation of IFNγ signaling. The surface area of the part of the tumor with necrotic/apoptotic cells was similar in the two CTL-treated groups (with or without anti-IFNγ mAb treatment), and the estimated number of dead cells was always smaller than that of the live cells (whether green or red; Fig. 4E). These results indicate that G_1 cell-cycle arrest, and not cytolytic killing, was primarily responsible for the CTL-induced suppression of tumor growth.

IFNγ directly suppress B16-fucci tumor cell growth through cell-cycle arrest

We constructed B16-fucci tumor cells expressing an IFNγ receptor lacking the intracellular component (B16-fucciΔIC). ACT did not suppress the growth of these cells even when 4-fold more CTLs (4×10^7) were transferred (Supplementary Fig. S2A). Although a similar number of CTLs infiltrated into B16-fucciΔIC tumor sites, as in mice with B16-fucci tumors receiving 4-fold less CTLs, no IFNγ production was observed (Supplementary Fig. S2B and S2C), and therefore the effect of IFNγ could not be evaluated in this system. This might be due to limited recognition of B16-fucciΔIC tumor cells by the CTL, because of their low level of MHC class I expression (Supplementary Fig. S2D). As expected, B16-fucciΔIC did not upregulate MHC class I molecules after exposure to IFNγ.

Because we could not evaluate the effect of IFNγ on tumor cells *in vivo* in this manner, we tested its effects directly on B16 tumor cells *in vitro*. As shown in Fig. 5, proliferation of B16-fucci cells, but not B16-fucciΔIC cells, was inhibited completely when they were treated with IFNγ (Fig. 5A). These cells were arrested in G_1 (Fig. 5B), showing that IFNγ directly inhibits the growth of B16-fucci tumor cells through G_1 cell-cycle arrest.

Recently, it was reported that a combination of IFNγ and TNFα produced by $CD4^+$ T cells can drive tumor cells into senescence by inducing $G_0–G_1$ cell-cycle arrest through the activation of p16INK4a (14). Therefore, we tested the effect of IFNγ and/or

Published OnlineFirst August 15, 2014; DOI: 10.1158/2326-6066.CIR-14-0098

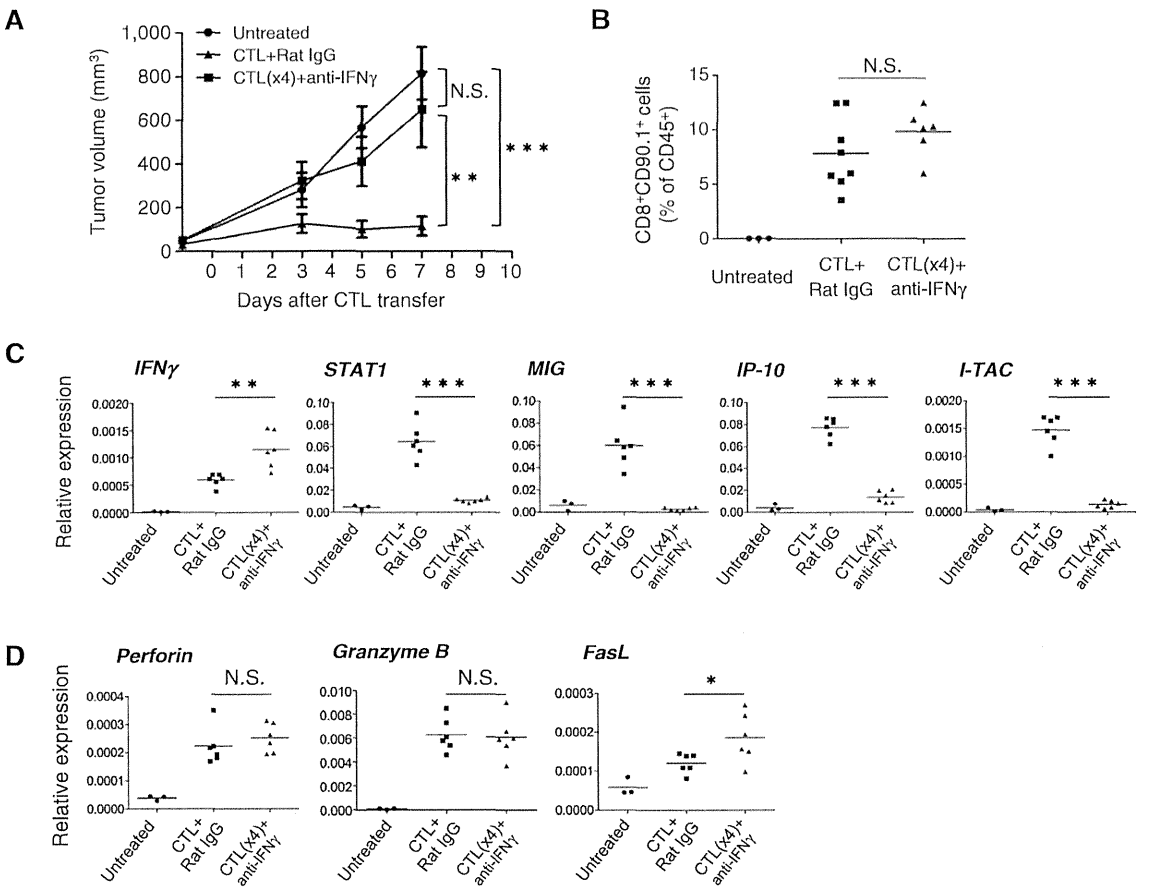

Figure 3.

IFNγ is critical for tumor growth inhibition. A, C57BL/6 mice were injected with B16-fucci tumor cells. Tumor-bearing mice ($n = 5$) were treated as described in Fig. 1, and anti-IFNγ or control rat IgG antibodies were injected intraperitoneally on days 0 and 2 after CTL transfer. Tumor volumes were measured on days 3, 5, and 7 after CTL transfer ($n = 5$). B, the frequency of CTLs ($CD45^+$ $CD90.1^+$ $CD8^+$) was assessed by flow cytometry. Tumors were harvested from each group on day 3 after CTL transfer. C and D, total RNA was isolated from tumor tissues and reverse-transcribed into cDNA. Expression of IFNγ-related genes (*IFNγ*, *STAT1*, *MIG*, *IP-10*, and *I-TAC*; C) and cytotoxicity-related genes (*Perforin*, *Granzyme B*, and *FasL*; D) was determined by qRT-PCR. *GAPDH* was used as an internal control. Samples were compared using an unpaired, two-tailed Student *t* test (*, $P < 0.05$; **, $P < 0.01$; and ***, $P < 0.001$; N.S., not statistically significant).

TNFα on B16 tumor cells. Whereas IFNγ alone inhibited cell proliferation by G_1 arrest, TNFα alone had a limited inhibitory effect on B16 proliferation even at a high concentration (10 ng/mL; Supplementary Fig. S3). When B16 tumor cells were cultured in the presence of both IFNγ and TNFα at a high concentration, a synergistic effect on cell growth inhibition and cell senescence was observed (Supplementary Fig. S3).

IFNγ production by transferred CTLs induces G_1 cell-cycle arrest by a mechanism involving Skp2/p27-related cell-cycle regulation

We next investigated the mechanism of G_1 cell-cycle arrest by IFNγ. B16-fucci tumor tissues were harvested from untreated mice, ACT mice treated with rat IgG, or ACT mice treated with anti-IFNγ mAb on day 3 after CTL transfer. Proteins were extracted from each tissue for Western blot analysis. As shown in Fig. 6A, downstream of IFNγ signaling, STAT1 was phosphorylated in tumors from ACT mice treated with rat IgG, but not in tumors from anti-IFNγ mAb-treated ACT mice. To confirm the gene expression data that *Skp2* was significantly downregulated in tumors from ACT mice (Fig. 1B and C), we examined the protein expression of Skp2. As shown in Fig. 6A, Skp2 expression was suppressed in tumors from control ACT mice, but not in those from mice treated with anti-IFNγ mAb. Conversely, the cyclin-dependent kinase inhibitor (CKI) p27 accumulated in the former but not in the latter. We also investigated the ataxia telangiectasia mutated (ATM)–p53–p21 pathway involved in G_1 cell-cycle arrest following DNA damage. We found that ATM was not upregulated as a result of CTL therapy, p53 was not activated, and no subsequent accumulation of p21 was observed. This shows that the ATM–p53–p21 pathway is not involved in this model (Fig. 6A). We also investigated the expression of these molecules *in vitro* (Fig. 6B). B16-fucci and B16-fucciΔIC tumor cells were treated with 10 U/mL IFNγ and

Published OnlineFirst August 15, 2014; DOI: 10.1158/2326-6066.CIR-14-0098

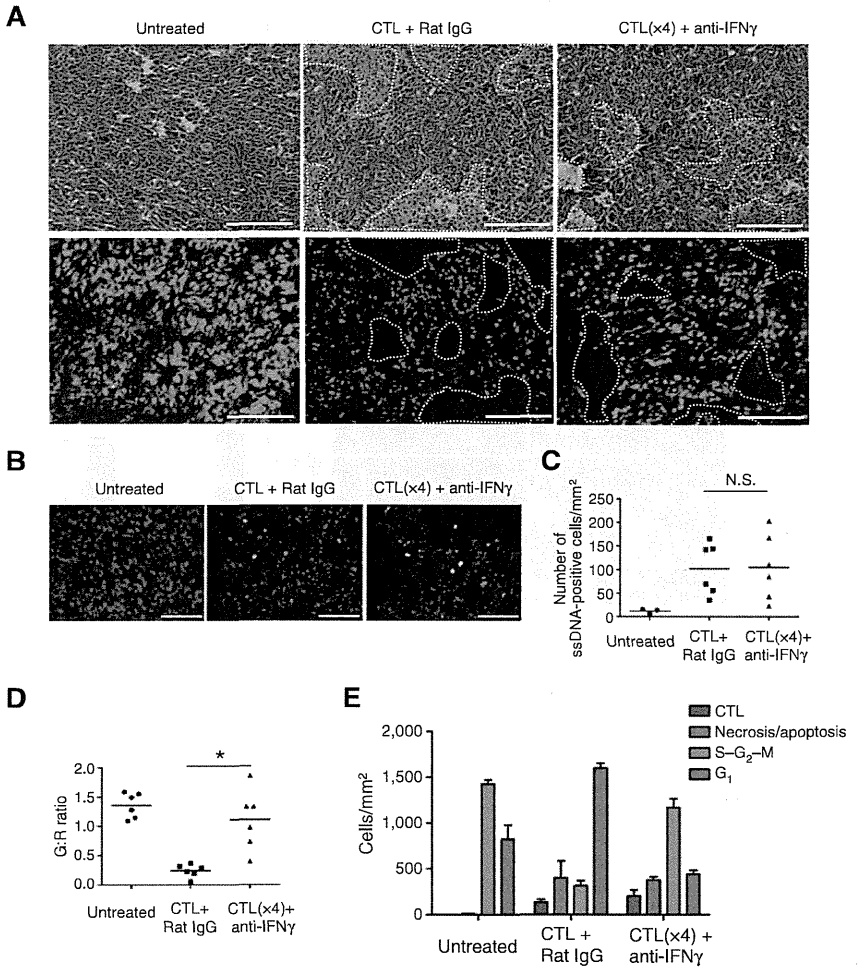

Figure 4.
CTLs block tumor growth by both lytic activity and IFNγ-dependent cell-cycle arrest. A, B16-fucci tumor-bearing mice ($n = 3$) were treated as described in Fig. 3. Hematoxylin and eosin (top) and fluorescence microscopy images (bottom) of frozen tumor sections on day 3 are shown. Dotted yellow lines, necrotic areas. Scale bars, 200 μm. B, apoptotic cells positive for ssDNA are shown in fluorescence microscopy images on day 3. Cells were counterstained with DAPI. Scale bars, 100 μm. C, quantification of ssDNA-positive cells within tumors. Numbers of ssDNA-positive cells were counted in five random fields of view. Data are expressed as the means ± SE of untreated mice ($n = 3$) and ACT mice injected with rat IgG ($n = 6$) or anti-IFNγ mAb ($n = 6$). D, analysis of the cell cycle was performed by calculating the G:R ratio in fluorescence images ($n = 6$ per group). E, the number of CTLs, tumor cells in necrotic areas, and tumor cells in G_1 or S–G_2–M. The number of cells in necrotic areas was estimated by calculating the surface area of the region using BZ-H1M software (Keyence). Total number of cells in at least three random fields of view (per mm^2) is shown. Representative data of 3 mice for each group are given. Samples were compared using an unpaired, two-tailed Student t test (*, $P < 0.01$; N.S., not statistically significant).

harvested at the indicated times. STAT1 phosphorylation was observed at early time points (15 and 30 minutes after IFNγ treatment) in B16-fucci, but not in B16-fucciΔIC. Skp2 expression was downregulated gradually, and p27 accumulated by 48 hours after IFNγ treatment in B16-fucci but not in B16-fucciΔIC cells (Fig. 6B). We confirmed that the ATM–p53–p21 pathway was also not involved in G_1 cell-cycle arrest *in vitro*. These results suggest that G_1 cell-cycle arrest by CTL therapy is likely due to Skp2/p27-related cell-cycle regulation by IFNγ.

Inhibition of FBL3 cell proliferation by IFNγ

We next investigated whether proliferation of other murine cell lines is inhibited by IFNγ. FBL3, p815, CT26, 3LL, and EL4 tumor cells were treated with IFNγ (10 U or 100 U/mL) for 4 to 6 days (Fig. 7A). The proliferation of FBL3 tumor cells was inhibited by IFNγ treatment in a manner similar to that of B16 tumor cells. The proliferation of P815, CT26, and 3LL tumor cells was moderately inhibited. No inhibition was observed in IFNγ-treated EL4 tumor cells. In Western blot analyses, using tumor lysates from FBL3 and EL4 tumors at the indicated time point, Stat1 phosphorylation was observed in FBL3 lysates, but the phosphorylation was very weak in EL4 tumor lysates. Skp2 expression was downregulated 24 to 48 hours after IFNγ treatment in FBL3 but not in EL4 tumors, and p27 accumulated (Fig. 7B). Again, the ATM–p53–p21 pathway was not involved. These results suggest that inhibition of FBL3 tumor cell proliferation by IFNγ might involve Skp2/p27-related cell-cycle regulation, as in B16.

Discussion

In this study, we demonstrated that the mechanism of tumor growth inhibition by adoptive CTL therapy was largely dependent on IFNγ-induced G_1 cell-cycle arrest rather than on tumor cell lysis. In microarray analysis, the upregulation of genes related to $CD8^+$ T cells, the MHC class I pathway, IFNγ signaling, cytotoxic effector molecules, and others was observed in tumors from ACT mice. At the same time, a decrease was found in the expression of some genes positively regulating the cell cycle in these tumors. Therefore, we focused on cell-cycle control in the B16 adoptive immunotherapy model and used the fucci system, which allows the visualization of cell-cycle stage of tumor cells *in situ* in mice receiving CTL.

Published OnlineFirst August 15, 2014; DOI: 10.1158/2326-6066.CIR-14-0098

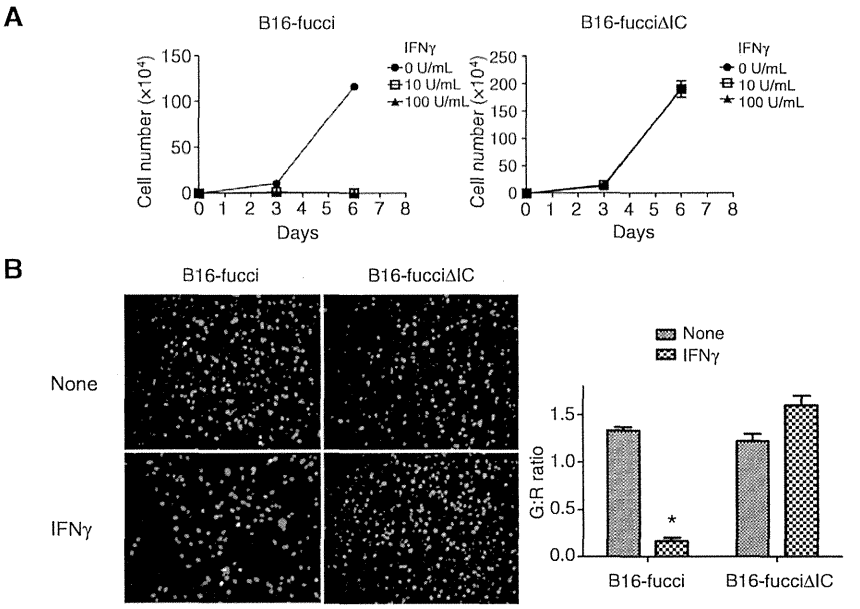

Figure 5.
IFNγ directly inhibits tumor cell growth through G_1 cell-cycle arrest. A, proliferation of B16-fucci cells or B16-fucci expressing an IFNγ receptor lacking the intracellular component (B16-fucciΔIC) was assessed after exposure to IFNγ (10 U/mL) for 6 days. B, B16-fucci or B16-fucciΔIC cells were incubated with IFNγ (10 U/mL). Two days later, the cell-cycle state was determined by fluorescence microscopy (left). Original magnification, ×200. The G:R ratio in fluorescence images is shown ($n = 2$ per group; right). Samples were compared using an unpaired, two-tailed Student t test (*, $P < 0.01$).

Histologic analysis following ACT showed that the number of CTLs in the tumor was far lower than that of tumor cells. On average, only 140 CTLs per mm^2 tumor tissue on day 3 after transfer were found. In contrast, this area contained 1,911 tumor cells (both green and red cells). Thus, it seems *a priori* unlikely that this small number of CTLs infiltrating the tumor would be sufficient to prevent tumor growth by direct cytotoxicity 3 to 7 days after CTL injection. Consistent with this observation, we also found that the area of the tumor undergoing necrosis/apoptosis was relatively small. Instead, a larger area consisting of tumor cells had undergone cell-cycle arrest at G_1. Therefore, transient tumor suppression from days 3 to 7 seems to be largely due to cell-cycle arrest rather than due to CTL killing. Using mAbs that neutralize IFNγ and completely block IFNγ signaling, we demonstrated that IFNγ is required for tumor growth inhibition and G_1 cell-cycle arrest but not for CTL killing. Thus, IFNγ-dependent G_1 cell-cycle arrest makes a major contribution to tumor growth suppression in this model. This would explain why tumor growth was suppressed despite the low ratio of CTLs to tumor cells in this system, and how T cells can suppress the growth of bystander tumor cells that may not express the target antigen. This could also explain some examples to tumor suppression by $CD4^+$ T cells that can also make IFNγ even if they are not lytic and even if the tumor is MHC class II negative, as long as antigen-presenting cells are infiltrating and can present antigen, as the soluble IFNγ can target neighboring cells.

IFNγ inhibits cell proliferation via cell type–specific pathways that involve CKIs, such as p21Cip1 (29, 30) and p27Kip1 (31, 32). It has been shown that STAT1 interacts directly with cyclin D1/Cdk4 and mediates the cell-cycle arrest of human U3A cells (33). Here, we investigated the involvement of CKIs in G_1 cell-cycle arrest, and found that p27Kip1, but not p21Cip1, accumulated in B16 tumor cells following CTL therapy *in vivo* or IFNγ treatment *in vitro*. Another CKI, p16, is involved in senescence-like G_1 cell-cycle arrest (14), but this factor is not expressed in B16 tumor cells due to a $p16^{Ink4a}$ exon1α deletion (34). Thus, p27Kip1 appeared to be the major CKI involved in G_1 arrest in this model. *Skp2* is an oncogene; Skp2 inactivation induces cell senescence independent

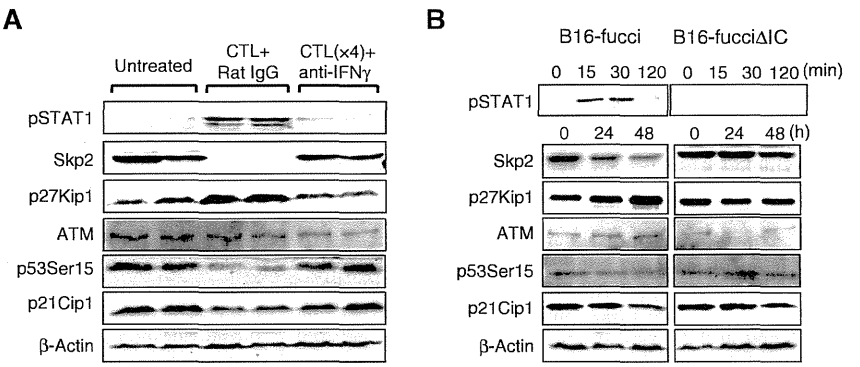

Figure 6.
G_1 cell-cycle arrest by ACT was mediated by IFNγ-dependent Skp2/p27-related cell-cycle regulation. A, B16-fucci tumors were harvested from untreated or ACT mice given control rat IgG or anti-IFNγ mAb on day 3 after CTL transfer. Protein extracts (50 μg) from tumor tissues in each group were used for immunoblotting of the indicated proteins. B, protein extracts from B16-fucci or B16-fucciΔIC cells treated with IFNγ (10 U/mL) for the indicated time were used for immunoblotting of the indicated proteins.

Published OnlineFirst August 15, 2014; DOI: 10.1158/2326-6066.CIR-14-0098

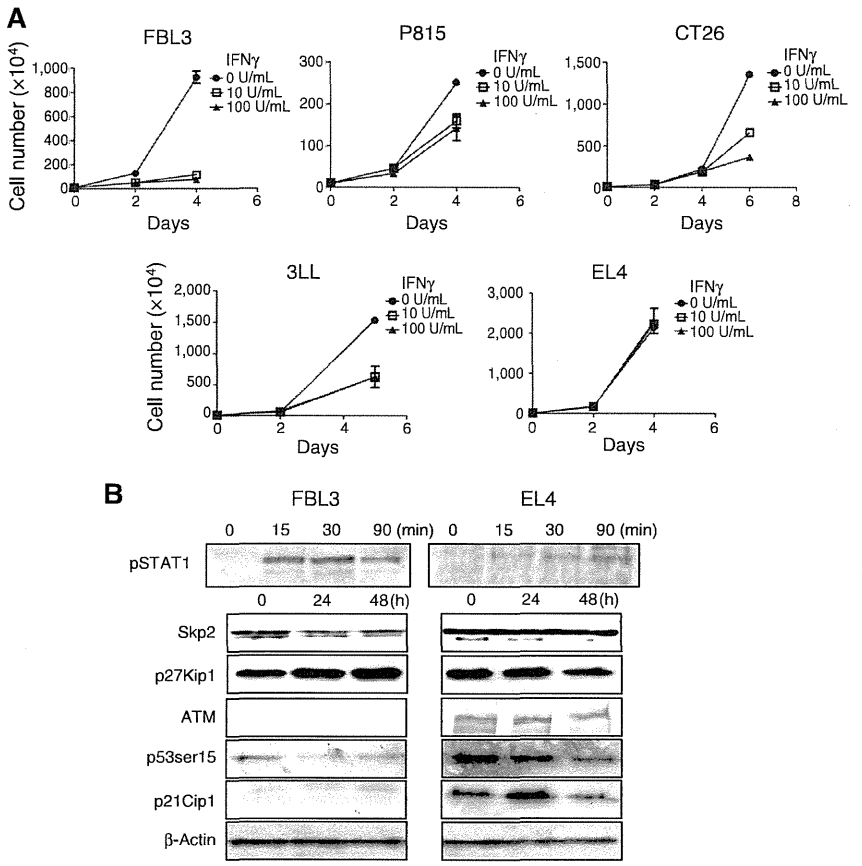

Figure 7.
Inhibition of cell proliferation by IFNγ in other murine cell lines. A, proliferation of FBL3, P815, CT26, 3LL, and EL4 cells after treatment with IFNγ (10 or 100 U/mL) for 4 to 6 days. B, protein extracts from FBL3 and EL4 cells treated with IFNγ (10 U/mL) for the indicated time were used for immunoblotting of the indicated proteins.

of the p53 pathway (35). STAT1 has been shown to repress *Skp2* gene transcription by binding to its promoter region and stabilizing p27Kip1 in Ras-transformed cells (36). In this report, we showed that Skp2 expression was downregulated after either CTL therapy or IFNγ treatment; thus, STAT1 may repress Skp2 expression and promote p27Kip1 stabilization.

G_1 cell-cycle arrest is also known to be induced by ATM-dependent activation of p53 and induction of p21Cip1 (37). Because ATM is a key molecule in the cellular response to DNA damage (38), we investigated its expression by Western blot analysis. We found that the ATM protein was not highly expressed in the tumor after CTL therapy. We also confirmed this finding *in vitro* in B16 cells cultured with IFNγ. Furthermore, p53 was not phosphorylated at Ser15, and the CKI p21Cip1, which is downstream of phospho-p53 (Ser15), was not upregulated. Therefore, we conclude that ATM expression and the subsequent activation of the phospho-p53–p21 pathway was not involved in this model.

We tested the effect of IFNγ on other murine tumor cell lines, and found that the proliferation of FBL-3 cells was strongly inhibited by IFNγ, similar to that of the B16 tumor cells. On the other hand, EL-4 cells were insensitive to IFNγ, whereas p815, CT26, and 3LL cells were moderately sensitive. IFNγ sensitivity and the mechanisms involved in the inhibition of cell proliferation may differ in different tumor cell lines. It is important to know whether IFNγ insensitivity is due to the downregulation of IFNγ receptors on these tumors, or defects in their IFNγ signal transduction.

Braumuller and colleagues (14) reported that IFNγ together with TNFα reduced the proliferation of different cancer cell lines in both mice and humans. Here, we showed that the combination of IFNγ and TNFα strongly inhibited B16 tumor cell proliferation and induced cell senescence (Supplementary Fig. S3). Because pmel-1 CTLs produce large amounts of IFNγ, but not TNFα, when they are cultured with B16 tumor cells *in vitro* (Supplementary Fig. S4), and IFNγ alone is enough to suppress tumor cell proliferation (Supplementary Fig. S3), the transient suppression of tumor growth from days 3 to 7 *in vivo* in this model may be entirely due to IFNγ, as there is only a small amount of TNFα at the tumor site. Th1 $CD4^+$ T cells or Toll-like receptor (TLR)–stimulated macrophages might be able to produce enough TNFα, but these cells are not present in our system. Alternatively, a strategy to induce polyfunctional $CD8^+$ T cells producing IFNγ, TNFα, and IL2 might be important to enhance further the antitumor effects in this model (39, 40).

IFNγ is a critical molecule in cancer immunosurveillance or immunoediting in primary mouse tumor models (41–44). In our study, as long as high concentrations of IFNγ were present

Published OnlineFirst August 15, 2014; DOI: 10.1158/2326-6066.CIR-14-0098

in the tumor, its growth was controlled through G_1 arrest (Supplementary Fig. S1). Thus, our study suggests that deregulation of the cell cycle due to insufficient availability of IFNγ or IFNγ insensitivity developed by tumor cells may be one mechanism by which tumor cells escape from CTL therapy (Supplementary Figs. S1 and S2).

Our study indicates that a small number of infiltrated CTLs can cause a large number of tumor cells to arrest in G_1 rather than dying. On the basis of this finding, we propose that the development of an appropriate strategy to maintain tumor cells in a quiescent, dormant state for extended periods (immunotherapy-induced equilibrium/dormancy), or to induce apoptosis/senescence, would be highly desirable.

Disclosure of Potential Conflicts of Interest

No potential conflicts of interest were disclosed.

Authors' Contributions

Conception and design: H. Matsushita, R. Maekawa, K. Kakimi
Development of methodology: M. Tomura, K. Kakimi
Acquisition of data (provided animals, acquired and managed patients, provided facilities, etc.): H. Matsushita, A. Hosoi, S. Ueha, J. Abe, N. Fujieda, R. Maekawa, O. Ohara, K. Kakimi
Analysis and interpretation of data (e.g., statistical analysis, biostatistics, computational analysis): H. Matsushita, A. Hosoi, S. Ueha, N. Fujieda, O. Ohara, K. Kakimi
Writing, review, and/or revision of the manuscript: H. Matsushita, K. Kakimi
Administrative, technical, or material support (i.e., reporting or organizing data, constructing databases): O. Ohara
Study supervision: K. Matsushima, K. Kakimi

Acknowledgments

The authors thank Dr. N. Restifo (National Cancer Institute) for providing the B16F10 tumor cell line, Dr. A. Miyawaki (RIKEN, Wako) for the Fucci system, and Mr. K. Sato (Kazusa DNA Research Institute) for excellent technical assistance in gene expression analysis.

Grant Support

This study was supported in part by a Grant-in-Aid for Scientific Research of the Ministry of Education, Culture, Sports, Science and Technology of Japan (K. Kakimi).

The costs of publication of this article were defrayed in part by the payment of page charges. This article must therefore be hereby marked *advertisement* in accordance with 18 U.S.C. Section 1734 solely to indicate this fact.

Received May 16, 2014; revised July 22, 2014; accepted August 5, 2014; published OnlineFirst August 15, 2014.

References

1. Rosenberg SA, Restifo NP, Yang JC, Morgan RA, Dudley ME. Adoptive cell transfer: a clinical path to effective cancer immunotherapy. Nat Rev Cancer 2008;8:299–308.
2. Morgan RA, Dudley ME, Wunderlich JR, Hughes MS, Yang JC, Sherry RM, et al. Cancer regression in patients after transfer of genetically engineered lymphocytes. Science 2006;314:126–9.
3. Brenner MK, Heslop HE. Adoptive T cell therapy of cancer. Curr Opin Immunol 2010;22:251–7.
4. Kalos M, Levine BL, Porter DL, Katz S, Grupp SA, Bagg A, et al. T cells with chimeric antigen receptors have potent antitumor effects and can establish memory in patients with advanced leukemia. Sci Transl Med 2011;3:95ra73.
5. Robbins PF, Morgan RA, Feldman SA, Yang JC, Sherry RM, Dudley ME, et al. Tumor regression in patients with metastatic synovial cell sarcoma and melanoma using genetically engineered lymphocytes reactive with NY-ESO-1. J Clin Oncol 2011;29:917–24.
6. Vierboom MP, Nijman HW, Offringa R, van der Voort EI, van Hall T, van den Broek L, et al. Tumor eradication by wild-type p53-specific cytotoxic T lymphocytes. J Exp Med 1997;186:695–704.
7. Hanson HL, Donermeyer DL, Ikeda H, White JM, Shankaran V, Old LJ, et al. Eradication of established tumors by CD8+ T cell adoptive immunotherapy. Immunity 2000;13:265–76.
8. Mukherjee P, Ginardi AR, Tinder TL, Sterner CJ, Gendler SJ. MUC1-specific cytotoxic T lymphocytes eradicate tumors when adoptively transferred *in vivo*. Clin Cancer Res 2001;7:848s–55s.
9. Kagi D, Vignaux F, Ledermann B, Burki K, Depraetere V, Nagata S, et al. Fas and perforin pathways as major mechanisms of T cell-mediated cytotoxicity. Science 1994;265:528–30.
10. Spiotto MT, Rowley DA, Schreiber H. Bystander elimination of antigen loss variants in established tumors. Nat Med 2004;10:294–8.
11. Breart B, Lemaitre F, Celli S, Bousso P. Two-photon imaging of intratumoral CD8+ T cell cytotoxic activity during adoptive T cell therapy in mice. J Clin Invest 2008;118:1390–7.
12. Zhang B, Karrison T, Rowley DA, Schreiber H. IFN-gamma- and TNF-dependent bystander eradication of antigen-loss variants in established mouse cancers. J Clin Invest 2008;118:1398–404.
13. Muller-Hermelink N, Braumuller H, Pichler B, Wieder T, Mailhammer R, Schaak K, et al. TNFR1 signaling and IFN-gamma signaling determine whether T cells induce tumor dormancy or promote multistage carcinogenesis. Cancer Cell 2008;13:507–18.
14. Braumuller H, Wieder T, Brenner E, Assmann S, Hahn M, Alkhaled M, et al. T-helper-1-cell cytokines drive cancer into senescence. Nature 2013;494:361–5.
15. Dunn GP, Koebel CM, Schreiber RD. Interferons, immunity and cancer immunoediting. Nat Rev Immunol 2006;6:836–48.
16. Winter H, Hu HM, McClain K, Urba WJ, Fox BA. Immunotherapy of melanoma: a dichotomy in the requirement for IFN-gamma in vaccine-induced antitumor immunity versus adoptive immunotherapy. J Immunol 2001;166:7370–80.
17. Liao F, Rabin RL, Yannelli JR, Koniaris LG, Vanguri P, Farber JM. Human Mig chemokine: biochemical and functional characterization. J Exp Med 1995;182:1301–14.
18. Luster AD, Leder P. IP-10, a -C-X-C- chemokine, elicits a potent thymus-dependent antitumor response *in vivo*. J Exp Med 1993;178:1057–65.
19. Cole KE, Strick CA, Paradis TJ, Ogborne KT, Loetscher M, Gladue RP, et al. Interferon-inducible T cell alpha chemoattractant (I-TAC): a novel non-ELR CXC chemokine with potent activity on activated T cells through selective high affinity binding to CXCR3. J Exp Med 1998;187:2009–21.
20. Bromberg JF, Horvath CM, Wen Z, Schreiber RD, Darnell JE Jr. Transcriptionally active Stat1 is required for the antiproliferative effects of both interferon alpha and interferon gamma. Proc Natl Acad Sci U S A 1996;93:7673–8.
21. Chin YE, Kitagawa M, Su WC, You ZH, Iwamoto Y, Fu XY. Cell growth arrest and induction of cyclin-dependent kinase inhibitor p21 WAF1/CIP1 mediated by STAT1. Science 1996;272:719–22.
22. Meurs E, Chong K, Galabru J, Thomas NS, Kerr IM, Williams BR, et al. Molecular cloning and characterization of the human double-stranded RNA-activated protein kinase induced by interferon. Cell 1990;62:379–90.
23. Deiss LP, Feinstein E, Berissi H, Cohen O, Kimchi A. Identification of a novel serine/threonine kinase and a novel 15-kD protein as potential mediators of the gamma interferon-induced cell death. Genes Dev 1995;9:15–30.
24. Noji S, Hosoi A, Takeda K, Matsushita H, Morishita Y, Seto Y, et al. Targeting spatiotemporal expression of CD137 on tumor-infiltrating cytotoxic T lymphocytes as a novel strategy for agonistic antibody therapy. J Immunother 2012;35:460–72.
25. Sakaue-Sawano A, Kurokawa H, Morimura T, Hanyu A, Hama H, Osawa H, et al. Visualizing spatiotemporal dynamics of multicellular cell-cycle progression. Cell 2008;132:487–98.

Published OnlineFirst August 15, 2014; DOI: 10.1158/2326-6066.CIR-14-0098

26. Dighe AS, Richards E, Old LJ, Schreiber RD. Enhanced *in vivo* growth and resistance to rejection of tumor cells expressing dominant negative IFN gamma receptors. Immunity 1994;1:447–56.
27. Ranganath S, Ouyang W, Bhattarcharya D, Sha WC, Grupe A, Peltz G, et al. GATA-3-dependent enhancer activity in IL-4 gene regulation. J Immunol 1998;161:3822–6.
28. Hosoi A, Matsushita H, Shimizu K, Fujii SI, Ueha S, Abe J, et al. Adoptive cytotoxic T lymphocyte therapy triggers a counter-regulatory immunosuppressive mechanism via recruitment of myeloid-derived suppressor cells. Int J Cancer 2014;134:1810–22.
29. Hobeika AC, Etienne W, Torres BA, Johnson HM, Subramaniam PS. IFN-gamma induction of p21(WAF1) is required for cell cycle inhibition and suppression of apoptosis. J Interferon Cytokine Res 1999;19:1351–61.
30. Gooch JL, Herrera RE, Yee D. The role of p21 in interferon gamma-mediated growth inhibition of human breast cancer cells. Cell Growth Differ 2000;11:335–42.
31. Harvat BL, Seth P, Jetten AM. The role of p27Kip1 in gamma interferon-mediated growth arrest of mammary epithelial cells and related defects in mammary carcinoma cells. Oncogene 1997;14:2111–22.
32. Lee SH, Kim JW, Oh SH, Kim YJ, Rho SB, Park K, et al. IFN-gamma/IRF-1-induced p27kip1 down-regulates telomerase activity and human telomerase reverse transcriptase expression in human cervical cancer. FEBS Lett 2005;579:1027–33.
33. Dimco G, Knight RA, Latchman DS, Stephanou A. STAT1 interacts directly with cyclin D1/Cdk4 and mediates cell cycle arrest. Cell Cycle 2010;9:4638–49.
34. Melnikova VO, Bolshakov SV, Walker C, Ananthaswamy HN. Genomic alterations in spontaneous and carcinogen-induced murine melanoma cell lines. Oncogene 2004;23:2347–56.
35. Lin HK, Chen Z, Wang G, Nardella C, Lee SW, Chan CH, et al. Skp2 targeting suppresses tumorigenesis by Arf-p53-independent cellular senescence. Nature 2010;464:374–9.
36. Wang S, Raven JF, Koromilas AE. STAT1 represses Skp2 gene transcription to promote p27Kip1 stabilization in Ras-transformed cells. Mol Cancer Res 2010;8:798–805.
37. Delia D, Fontanella E, Ferrario C, Chessa L, Mizutani S. DNA damage-induced cell-cycle phase regulation of p53 and p21waf1 in normal and ATM-defective cells. Oncogene 2003;22:7866–9.
38. Kitagawa R, Kastan MB. The ATM-dependent DNA damage signaling pathway. Cold Spring Harb Symp Quant Biol 2005;70:99–109.
39. Perret R, Ronchese F. Effector CD8+ T cells activated *in vitro* confer immediate and long-term tumor protection *in vivo*. Eur J Immunol 2008;38:2886–95.
40. Imai N, Ikeda H, Tawara I, Shiku H. Tumor progression inhibits the induction of multifunctionality in adoptively transferred tumor-specific CD8+ T cells. Eur J Immunol 2009;39:241–53.
41. Kaplan DH, Shankaran V, Dighe AS, Stockert E, Aguet M, Old LJ, et al. Demonstration of an interferon gamma-dependent tumor surveillance system in immunocompetent mice. Proc Natl Acad Sci U S A 1998;95:7556–61.
42. Shankaran V, Ikeda H, Bruce AT, White JM, Swanson PE, Old LJ, et al. IFNgamma and lymphocytes prevent primary tumour development and shape tumour immunogenicity. Nature 2001;410:1107–11.
43. Koebel CM, Vermi W, Swann JB, Zerafa N, Rodig SJ, Old LJ, et al. Adaptive immunity maintains occult cancer in an equilibrium state. Nature 2007;450:903–7.
44. Schreiber RD, Old LJ, Smyth MJ. Cancer immunoediting: integrating immunity's roles in cancer suppression and promotion. Science 2011;331:1565–70.

Published OnlineFirst August 15, 2014; DOI: 10.1158/2326-6066.CIR-14-0098

AACR American Association for Cancer Research

Cancer Immunology Research

Cytotoxic T Lymphocytes Block Tumor Growth Both by Lytic Activity and IFN γ-Dependent Cell-Cycle Arrest

Hirokazu Matsushita, Akihiro Hosoi, Satoshi Ueha, et al.

Cancer Immunol Res 2015;3:26-36. Published OnlineFirst August 15, 2014.

Tracking of intertissue migration reveals the origins of tumor-infiltrating monocytes

Francis H. W. Shand[a,b], Satoshi Ueha[a], Mikiya Otsuji[a], Suang Suang Koid[b,c], Shigeyuki Shichino[a], Tatsuya Tsukui[a], Mizuha Kosugi-Kanaya[a,d], Jun Abe[a], Michio Tomura[e], James Ziogas[b], and Kouji Matsushima[a,1]

[a]Department of Molecular Preventive Medicine, Graduate School of Medicine, The University of Tokyo, 7-3-1 Hongo, Bunkyo-ku, Tokyo 113-0033, Japan; [b]Department of Pharmacology and Therapeutics, The University of Melbourne, Parkville, Victoria 3010, Australia; [c]St. Vincent's Institute of Medical Research, Fitzroy, Victoria 3065, Australia; [d]Department of Hematology, Hokkaido University Graduate School of Medicine, Kita-15 Nishi-7, Kita-ku, Sapporo, Hokkaido 060-8638, Japan; and [e]Center for Innovation in Immunoregulative Technology and Therapeutics, Graduate School of Medicine, Kyoto University, Yoshidakonoe-cho, Sakyo-ku, Kyoto 606-8501, Japan

Edited by Frederic Geissmann, King's College London, London, United Kingdom, and accepted by the Editorial Board April 22, 2014 (received for review February 22, 2014)

Myeloid cells such as monocytes and monocyte-derived macrophages promote tumor progression. Recent reports suggest that extramedullary hematopoiesis sustains a sizable reservoir of tumor-infiltrating monocytes in the spleen. However, the influence of the spleen on tumor development and the extent to which spleen monocytes populate the tumor relative to bone marrow (BM) monocytes remain controversial. Here, we used mice expressing the photoconvertible protein Kikume Green-Red to track the redistribution of monocytes from the BM and spleen, and mice expressing fluorescent ubiquitination-based cell-cycle indicator proteins to monitor active hematopoiesis in these tissues. In mice bearing late-stage tumors, the BM, besides being the major site of monocyte production, supplied the expansion of the spleen reservoir, replacing 9% of spleen monocytes every hour. Deployment of monocytes was equally rapid from the BM and the spleen. However, BM monocytes were younger than those in the spleen and were 2.7 times more likely to migrate into the tumor from the circulation. Partly as a result of this intrinsic difference in migration potential, spleen monocytes made only a minor contribution to the tumor-infiltrating monocyte population. At least 27% of tumor monocytes had traveled from the BM in the last 24 h, compared with only 2% from the spleen. These observations highlight the importance of the BM as the primary hematopoietic tissue and monocyte reservoir in tumor-bearing mice, despite the changes that occur in the spleen monocyte reservoir during tumor development.

cancer immunity | tumor-associated macrophage | monocytopoiesis | KikGR | Fucci

Myeloid cells such as monocytes infiltrate almost all solid tumors (1). The presence of tumor-associated macrophages, which are derived directly from monocytes, correlates with poor prognosis (2, 3). These cells influence tumor progression through direct interactions with tumor cells, by modulating adaptive immune responses to the tumor, and by creating conditions that support angiogenesis, invasion, and metastasis (4–6). Understanding the origins and characteristics of tumor-infiltrating myeloid cells may lead to novel approaches to cancer therapy.

In healthy adult humans and mice, all myeloid cell formation occurs in the bone marrow (BM) (7). However, in certain disease states, organs such as the liver and spleen become sites of extramedullary hematopoiesis (8, 9). In tumor-bearing mice myeloid cells accumulate in the spleen (10–12), making this organ a candidate source of tumor-infiltrating cells. Recent reports propose that a rapidly mobilized reservoir of monocytes in the spleen contributes significant numbers of infiltrating cells in acute and chronic inflammatory conditions including myocardial infarction (13–15), stroke (14), atherosclerosis (15), and cancer (16, 17). In cancer, extramedullary hematopoiesis in the spleen is suggested to sustain a continuous supply of monocytes to the tumor (16, 17). These reports challenge the classical view of the BM as the primary site of monocyte production and supply (18). Current approaches to measuring tissue origin and migration include BrdU labeling, adoptive transfer, tissue transplantation, and parabiosis experiments. However, it has remained difficult to assess accurately the relative contributions of different pools of myeloid cells to the tumor-infiltrating monocyte population (16).

In the present study, we developed methods using mice expressing the photoconvertible protein Kikume Green-Red (KikGR) (19, 20) or fluorescent ubiquitination-based cell cycle indicator (Fucci) proteins (21, 22), which enabled us to compare the BM and spleen monocyte pools directly in terms of supply and production. We demonstrate that spleen-pool monocytes make only a minor contribution to the tumor-infiltrating monocyte population, partly because BM-pool monocytes have an intrinsic migration advantage over their spleen-pool counterparts.

Results

Spleen Monocyte Cellularity Increases Only in Late-Stage Tumor Development. To characterize the relationship between tumor growth and the expansion of the spleen monocyte pool in tumor-bearing mice, we inoculated Lewis lung carcinoma (3LL) tumor cells s.c. into the flanks of wild-type mice. This syngeneic transplant model yields reproducible nodular tumor growth in immunocompetent hosts with minimal metastasis, facilitating quantitative

Significance

Solid tumors contain large numbers of immune cells, including monocytes and monocyte-derived macrophages that promote tumor progression. During tumor development, monocytes accumulate in the spleen. However, the influence of spleen cells on tumor growth remains controversial. Here, we used novel methods for tracking intertissue migration and monitoring hematopoiesis to show that during tumor development the bone marrow dramatically accelerates production of monocytes, rapidly transferring many of these newly formed cells to a reservoir in the spleen. However, these spleen monocytes are less able than their bone marrow counterparts to enter the tumor and make only a minor contribution to the tumor-infiltrating monocyte population. These findings clarify the roles of the spleen and bone marrow in cancer development.

Author contributions: F.H.W.S., S.U., M.T., and K.M. designed research; F.H.W.S., S.U., S.S.K., S.S., T.T., and M.K.-K. performed research; M.T. contributed new reagents/analytic tools; F.H.W.S., S.U., and M.O. analyzed data; and F.H.W.S., S.U., M.O., S.S.K., S.S., T.T., M.K.-K., J.A., M.T., J.Z., and K.M. wrote the paper.

The authors declare no conflict of interest.

This article is a PNAS Direct Submission. F.G. is a guest editor invited by the Editorial Board.

Freely available online through the PNAS open access option.

[1]To whom correspondence should be addressed. E-mail: koujim@m.u-tokyo.ac.jp.

This article contains supporting information online at www.pnas.org/lookup/suppl/doi:10.1073/pnas.1402914111/-/DCSupplemental.

analysis of tumor tissue and infiltrating immune cells. Palpable solid tumors developed after 7 d with a dramatic increase in tumor growth after 28 d (Fig. S1 *A* and *B*) that coincided with increases in spleen weight (Fig. S1*C*), spleen monocyte cellularity (Fig. S1*D*), and blood monocyte numbers (Fig. S1*E*). We focused on the Ly6C^{hi} "inflammatory" monocyte subset because these cells make up the majority of the tumor-infiltrating monocyte population (23). The number of monocytes in the tumor peaked at day 21 (Fig. S1*F*), at the same time that a transient decrease in BM monocytes was observed (Fig. S1*D*). These data show that expansion of the spleen monocyte pool occurs only in late-stage tumor development, prompting us to focus on day-35 tumors in subsequent experiments.

Tumor-Infiltrating Monocytes Are Supplied Primarily from the BM Pool. To determine the contribution of the spleen to the tumor-infiltrating monocyte population, we used day-35 tumor-bearing BM chimeras in which myeloid cells expressed the green-to-red irreversibly photoconvertible protein KikGR (hereafter, "KikGR mice") (19, 20). By adapting previously developed methods that involve surgically irradiating selected tissues with violet light (24–27), we were able to timestamp monocytes present in the left femur (for monocytes of BM origin) or spleen and then track their redistribution throughout the body over a 24-h period using flow cytometry (Fig. 1 *A* and *B*). The procedure resulted in photoconversion of 25–40% of monocytes in either pool (Fig. 1*B* and Fig. S2*C*) without affecting cell viability or migration potential (Fig. S3 *A* and *C*). KikGR-Red (KikRed) protein levels remained stable for the duration of the experiments (Fig. S3*B*), and none of the results obtained by the KikGR approach were attributable to acute fluctuations in monocyte numbers following surgery. Femur photoconversion data were adjusted to represent the contribution of the whole-body BM pool, and all data were adjusted to simulate 100% photoconversion of source tissues, thus correcting for variations in photoconversion efficiency (see *Materials and Methods* for details).

After photoconversion, KikRed^{+} monocytes egressed rapidly from the BM and spleen (Fig. 1*C*) and appeared in the blood (Fig. 1*D*). Time-course graphs (Fig. 1 *C*–*E*) represent the redistribution of cells labeled KikRed^{+} at time 0 h as they move from source tissues (BM or spleen) to destination tissues (blood and tumor). A lesser proportion of photoconverted monocytes was retained in the spleen than in the BM (Fig. 1*C*; 6 h time point onwards), suggesting that monocyte replacement occurs more rapidly in the spleen pool. However, BM-pool KikRed^{+} monocytes outnumbered spleen-pool KikRed^{+} monocytes in the blood, in line with whole-body BM and spleen monocyte numbers (Table S1). Similar results were observed in non–tumor-bearing mice (Fig. S4 *A* and *B*).

Importantly, the KikGR approach enabled us to determine the extent of monocyte migration from pools in the BM and spleen to the tumor. BM-pool KikRed^{+} cells considerably outnumbered spleen-pool KikRed^{+} cells in the tumor, even at the peak of spleen-pool KikRed^{+} monocyte accumulation at 12 h (30×10^3 vs. 3×10^3) (Fig. 1*E*). From the peak numbers of KikRed^{+} cells that were detected in the tumor, we estimate that at least 27% (45×10^3) of tumor monocytes had traveled from the BM in the last 24 h compared with ~2% (3×10^3) from the spleen, not taking cell death or exit from the tumor into account (Fig. 1*E* and Table S1). Taken together, these results indicate that spleen-pool monocytes make a relatively minor contribution to the tumor-infiltrating monocyte population.

BM-Pool Monocytes Have a Migration Advantage over Spleen-Pool Monocytes. We next investigated possible causes for the dominance of BM-pool monocytes within the tumor. The accumulation of monocytes is influenced by the availability of monocytes from the BM or spleen, their ability to extravasate into the tumor, and the length of time that they are retained within the tumor. In tumor-bearing mice, the BM contains six times more monocytes than the spleen (Table S1). Surprisingly, however, our data still favored the accumulation in the tumor of BM-pool monocytes over spleen-pool monocytes, even when corrected for the greater availability of BM-pool monocytes in the body (Fig. 2*A*).

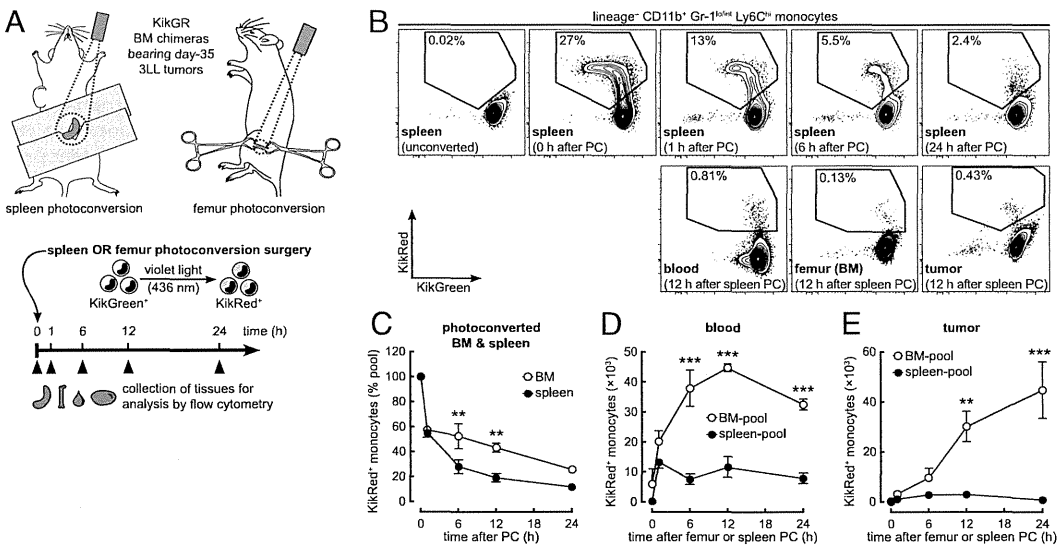

Fig. 1. Tumor-infiltrating monocytes are supplied primarily from the BM pool. (*A*) Surgical procedure and timeline for photoconversion experiments. The spleen or left femur of KikGR BM chimeras bearing day-35 3LL tumors was irradiated with violet light, resulting in the photoconversion of myeloid cell KikGreen protein to KikRed. (*B*) Representative flow cytometry plots showing the egress of photoconverted (KikRed^{+}) Ly6C^{hi} monocytes from the spleens of tumor-bearing mice and their redistribution to the blood, unconverted BM, and tumor (see Fig. S2*C* for BM egress plots). (*C*) Egress of KikRed^{+} Ly6C^{hi} monocytes from the BM and spleen after photoconversion. Data are expressed as a proportion of the initial pool of photoconverted cells in each tissue. (*D* and *E*) Accumulation of KikRed^{+} BM-pool and spleen-pool Ly6C^{hi} monocytes in the blood and tumor. PC, photoconversion. $^{**}P \leq 0.01$; $^{***}P \leq 0.001$ (BM-pool vs. spleen-pool). Data represent means ± SEM ($n = 3$) and are representative of two independent experiments.

This result suggested that additional factors might limit the potential of spleen-pool monocytes to accumulate in the tumor.

We therefore adopted a mathematical approach to quantify and compare the migration properties of tumor-infiltrating monocytes. Using weighted least squares regression analysis, equations modeling the entry and exit of cells to and from the tumor were fitted to blood and tumor KikGR time-course data (see *Materials and Methods* for details). Migration probability, the probability per unit time that a cell would migrate from the blood to the tumor, was 2.7-fold higher for BM-pool monocytes than for spleen-pool monocytes (Fig. 2*B*), whereas no significant difference was detected between the tumor residence times of cells from either pool (Fig. 2*C*). These results show that an intrinsic difference in the ability of monocytes from different pools to migrate from the blood to the tumor is at least partly responsible for the dominance of BM-pool monocytes within the tumor.

As an independent approach to compare the migration potential of BM-pool and spleen-pool monocytes, we examined the redistribution of cells from both sources after adoptive transfer of an equal mixture of these cells directly into the blood of tumor-bearing mice (Fig. 2*D*). Four hours after transfer, there still were equal numbers of donor BM and spleen monocytes in the blood (Fig. 2 *E* and *F*), but there was a higher proportion of BM-pool cells than spleen-pool cells in the recipient tumor (Fig. 2 *E* and *F*). These results support our conclusion that BM-pool monocytes extravasate into the tumor more readily than their spleen-pool counterparts because of an intrinsic difference in their migration potential.

The BM Is the Major Site of Monocyte Production in Tumor-Bearing Mice. Even if spleen-pool monocytes make only a minor contribution to the tumor-infiltrating monocyte population, it has been reported that the spleen plays a role in the production and development of monocytes in the tumor-bearing state (16, 17). To assess the relative contribution of the spleen to monocyte production in tumor-bearing mice, we used mice expressing Fucci proteins (hereafter, "Fucci mice") (21, 22) and flow cytometry to compare the extent of hematopoiesis occurring in the BM and spleen (Fig. 3*A*). In Fucci mice, Fucci-orange (mKO2) and Fucci-green (mAG) are expressed reciprocally in the G_1 and $S/G_2/M$ phases of the cell cycle, respectively. Because Fucci-green is degraded by ubiquitin-mediated proteolysis in late M phase, there is no carryover of green fluorescence to daughter cells. Numbers of actively proliferating (Fucci-green$^+$) hematopoietic stem cells (HSCs), granulocyte-macrophage progenitor (GMP) cells (committed precursors to the monocyte and neutrophil lineages), and monocytes were 10- to 100-fold higher in the spleen and were fivefold higher in the BM of day-33 tumor-bearing mice than in non–tumor-bearing mice (Fig. 3*B*). However, actively proliferating HSCs, GMP cells, and monocytes in the BM far outnumbered those in the spleen in both non–tumor-bearing and tumor-bearing mice (Fig. 3*B*). Furthermore, in tumor-bearing mice, 65% of BM monocytes (up from 21% in non–tumor-bearing mice) were actively proliferating, compared with only 16% of spleen monocytes (Fig. 3*C*).

Although mature monocytes are postmitotic (18), proliferating monocytes have been described in the BM of healthy mice and elsewhere in disease states (28–30). These immature cells have promonocyte morphology, express the cell surface proteins CD11b and Ly6C, and share functional similarities with mature monocytes. They are distinct from monoblast-like cells that do not express CD11b, including macrophage and dendritic cell precursors ("MDPs") and common monocyte progenitors ("cMoPs") (30, 31). Thus, the Fucci-green$^+$ Ly6C^{hi} cells observed in our experiments are likely to represent immature monocytes or promonocytes. Because the Fucci-orange fusion protein undergoes cell-cycle–dependent ubiquitination followed by proteolysis during the $S/G_2/M$ phases but accumulates during the G_1 phase, it provides an indication of the time elapsed since last cell division in Fucci-green$^-$ cells (22). Expression levels of Fucci-orange were lower in BM monocytes than in spleen and blood monocytes, indicating that the BM contains relatively younger cells (Fig. 3 *A* and *D*). Taken together, these results demonstrate that the BM is the major site of monocyte production in tumor-bearing mice.

The Supply of BM-Pool Monocytes to the Spleen Increases in the Tumor-Bearing State. The relatively low proportion of Fucci-green$^-$ (Fucci-orange$^+$) G_1/G_0-phase monocyte progeny observed in the BM of tumor-bearing mice suggests that many monocytes or promonocytes exit the BM while in the $S/G_2/M$ phase of the cell cycle (Fig. 3*C*). The number and proportion of Fucci-green$^+$ monocytes in the blood increased considerably in the tumor-bearing state (cell number increased by 100-fold) but remained much lower than in the spleen (Fig. 3 *B* and *C*). These data suggest either that monocytes/promonocytes are becoming Fucci-green$^+$ in the spleen or that Fucci-green$^+$ monocytes/promonocytes from the circulation are accumulating selectively in the spleen. Therefore we used femur photoconversion experiments to determine the extent to which the spleen pool is repopulated by BM monocytes. Monocytes moved continuously from the BM to the spleen, and in tumor-bearing mice, the accumulation of BM-pool KikRed$^+$ monocytes in the spleen increased substantially (Fig. 4*A*). Given that the size of the BM pool does not increase in tumor-bearing mice, this result demonstrates that a greater quantity and proportion of BM-pool monocytes migrate to the spleen in the tumor-bearing state. Our data suggest that in tumor-bearing mice, at least 9% (0.4×10^6) of spleen monocytes are replaced by BM-pool monocytes every hour (Fig. S4*D* and Table S1), not taking recirculation from the spleen into account.

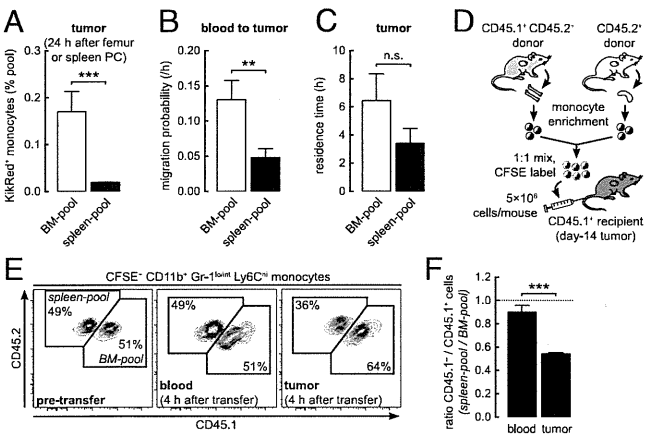

Fig. 2. BM-pool monocytes have a migration advantage over spleen-pool monocytes. (*A*) Accumulation of KikRed$^+$ monocytes in the tumor expressed relative to their abundance in respective source pools (see Fig. S4*C* for full time-course data). PC, photoconversion. (*B* and *C*) Weighted least squares regression analysis of KikRed$^+$ monocyte data was used to calculate blood-to-tumor migration probability (*B*) and tumor residence time (*C*). (*D*) BM or spleen cells from day-14 tumor-bearing donors were enriched for monocytes by lineage depletion before adoptive transfer into tumor-bearing recipients. (*E*) Representative flow cytometry plots showing donor spleen-derived [carboxyfluorescein succinimidyl ester (CFSE)$^+$ CD45.1$^-$] and donor BM-derived (CFSE$^+$ CD45.1$^+$) monocytes before and after transfer. (*F*) Ratio of donor spleen-derived to BM-derived monocytes in recipient tissues 4 h after transfer. n.s., not significant; $^{**}P \leq 0.01$; $^{***}P \leq 0.001$. Data represent means ± SEM ($n = 3$) in *A* and *F* or SE (30–39 degrees of freedom) in *B* and *C* and are representative of (*A*, *E*, and *F*) or are pooled from (*B* and *C*) two independent experiments.

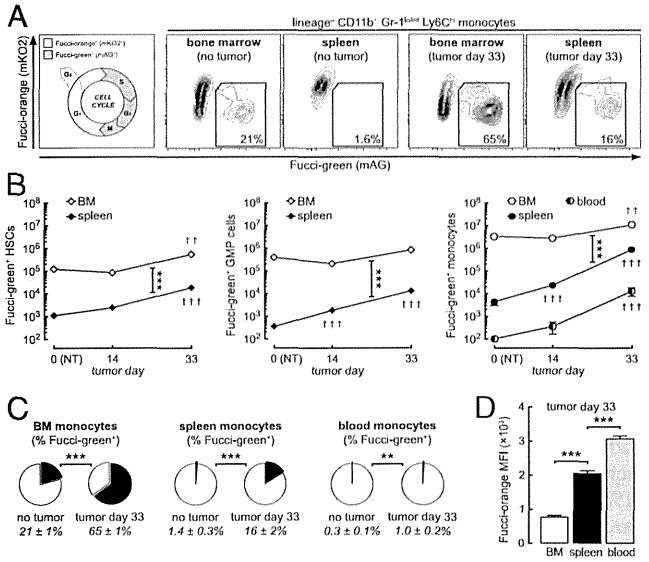

Fig. 3. The BM is the major site of monocyte production in tumor-bearing mice. (*A*) Representative flow cytometry plots showing actively proliferating Ly6C^{hi} monocytes (or promonocytes) in the BM and spleen of Fucci transgenic mice. (*B*) Actively proliferating (Fucci-green$^+$) lineage-negative c-kit$^+$ Sca-1$^+$ HSCs, lineage-negative c-kit$^+$ Sca-1$^-$ CD16/32$^+$ CD34$^+$ GMP cells, and Ly6C^{hi} monocytes in the BM, spleen, and whole-body blood of non–tumor-bearing (NT) and tumor-bearing mice (see Fig. S2*D* for flow cytometry gating). (*C*) Proportions of actively proliferating Ly6C^{hi} monocytes in the BM, spleen, and blood. (*D*) Expression levels (mean fluorescence intensity) of Fucci-orange in Fucci-green$^-$ monocytes from the BM, spleen, and blood of day-33 tumor-bearing mice. Fucci-orange accumulates during the G1 phase of the cell cycle, thus providing an indication of the time elapsed since last cell division. $^{**}P \leq 0.01$; $^{***}P \leq 0.001$ (comparisons as indicated). $^{\dagger\dagger}P \leq 0.01$; $^{\dagger\dagger\dagger}P \leq 0.001$ (compared with non–tumor-bearing control). Data represent means ± SEM (n = 6–8) and are representative of two independent experiments.

Femur photoconversion experiments also allowed us to measure the reentry of cells into the BM, because KikRed$^+$ monocytes that had egressed from the photoconverted femur could be detected in the opposite, unconverted femur. Fewer BM-pool KikRed$^+$ monocytes reentered the BM in tumor-bearing mice than in non–tumor-bearing mice (Fig. 4*B*), suggesting that in the tumor-bearing state most BM-pool monocytes are consumed in peripheral tissues such as the tumor and spleen, rather than returning to the BM. Taken together, our results show that increased monocyte production in the BM of tumor-bearing mice supplies the expansion of the spleen pool, partly through the rapid transfer of immature monocytes or promonocytes that continue to divide in the spleen.

Discussion

Tumor-infiltrating myeloid cells are short lived and are sustained by constant supply from the circulation (23). In this study we used KikGR and Fucci mice to compare the contributions of the BM and spleen as sources of tumor-infiltrating monocytes. We provide definitive evidence that monocytes from both the BM and spleen pools are deployed rapidly and continuously to the tumor. However, the vast majority of tumor-infiltrating monocytes were supplied from the BM pool, partly because BM-pool monocytes had an intrinsic migration advantage over spleen-pool monocytes. Moreover, the BM was the major site of monocyte production in tumor-bearing mice, and the rapid transfer of BM monocytes supplied the expansion of the spleen monocyte pool.

Our results demonstrate that, despite its fixed physical capacity, the BM is able to accelerate production of monocytes dramatically to meet demand. This accelerated monocytopoiesis occurs without any detectable increase in BM total cell number, suggesting that the newly produced cells overflow into the circulation rapidly. Short-pulse (≤12 h) BrdU labeling studies in tumor-bearing mice have shown that most myeloid cells populate peripheral tissues, including the spleen, only after expansion and mobilization from the BM (23). Our KikGR data confirm the rapid transfer of monocytes from the BM to the spleen and suggest that accelerated monocytopoiesis in the BM drives expansion of the spleen pool. Thus, although the spleen provides overflow capacity for the BM, it does not supplant the BM as the primary site of monocytopoiesis in tumor-bearing mice. The trigger for increased monocytopoiesis in the BM may be the increased consumption of monocytes by the tumor, because peak tumor monocyte infiltration at day 21 coincided with a transient drop in BM monocyte numbers. In addition, tumors can secrete long-range signals that activate hematopoietic cells in the BM (32, 33).

The basis for the difference in the migration potential of BM-pool and spleen-pool monocytes remains unclear. It seems unlikely that the splenic microenvironment influences monocyte function, because KikGR data show that the majority of monocytes in the spleen pass through only transiently. However, monocytes in the BM were younger than those in the spleen. Differences in the maturity of monocytes might result in differences in the expression of chemokine receptors, adhesion molecules, and survival factors that influence migration into and survival within inflammatory sites (34). For example, the chemokine receptor CCR2 mediates monocyte recruitment to the tumor (23, 35) and is required for monocyte egress from the BM but not from the spleen (13, 36). Selection for expression of CCR2 upon monocyte egress from the BM could provide these cells with a migration advantage over older spleen-pool monocytes that do not face similar selection upon egress to the circulation. Future studies should clarify the mechanistic basis for differences in the migration potential of monocytes from different pools.

KikGR and Fucci mice offer powerful, quantitative means for tracking intertissue cell migration and monitoring cell proliferation under steady-state conditions. Unlike adoptive transfer experiments in which cells prepared ex vivo are reinjected into the circulation en masse, the KikGR approach enables visualization of changes in supply over time, by revealing the gradual egress of specific cell populations from their source tissues and their accumulation in the circulation. Moreover, unlike tissue transplantation and parabiosis experiments, KikGR experiments cause minimal disruption of physiological conditions. By analyzing

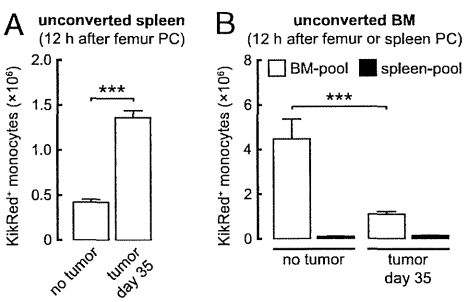

Fig. 4. The supply of BM-pool monocytes to the spleen increases in the tumor-bearing state. (*A*) Accumulation of KikRed$^+$ BM-pool Ly6C^{hi} monocytes in the unconverted spleen. (*B*) Accumulation of KikRed$^+$ BM-pool and spleen-pool Ly6C^{hi} monocytes in the unconverted BM. BM-pool data indicate the reentry of cells egressing from the opposite (photoconverted) femur. PC, photoconversion. See Fig. S4 *D* and *E* for full time-course data. $^{***}P \leq 0.001$. Data represent means ± SEM (n = 3) and are representative of two independent experiments.